Received: 8 November 2021 | Revised: 25 February 2022 | Accepted: 12 March 2022

DOI: 10.1111/jmg.12666

ORIGINAL ARTICLE

Journal of METAMORPHIC GEOLOGY WILEY

Abiotic passive nitrogen and methane enrichment during exhumation of subducted rocks: Primary multiphase fluid inclusions in high-pressure rocks from the Cabo Ortegal Complex, NW Spain

Tamás Spránitz[1] | José Alberto Padrón-Navarta[2,3] | Csaba Szabó[1,4] | Ábel Szabó[1] | Márta Berkesi[1,4]

[1]Lithosphere Fluid Research Lab, Department of Petrology and Geochemistry, Institute of Geography and Earth Sciences, Eötvös Loránd University, Budapest, Hungary

[2]Instituto Andaluz de Ciencias de la Tierra (IACT)-CSIC, Universidad de Granada, Granada, Spain

[3]Géosciences Montpellier, Université de Montpellier, Montpellier, France

[4]Institute of Earth Physics and Space Sciences, Eötvös Loránd Research Network (ELKH EPSS), Budapest, Hungary

Correspondence
Márta Berkesi, Institute of Earth Physics and Space Sciences, Eötvös Loránd Research Network (ELKH EPSS), 1112, Budapest, Meredek utca 18 Hungary
Email: berkesi.marta@epss.hu and marta.berkesi@ttk.elte.hu

Handling editor: Bernardo Cesare

Funding information
Nemzeti Kutatási Fejlesztési és Innovációs Hivatal (NKFIH); Ramón y Cajal fellowship

Abstract

Primary multiphase fluid inclusions (MFI) were studied in one eclogite and two granulites from the Cabo Ortegal Complex (COC, NW Spain) by means of Raman imaging, Scanning Electron Microscopy with Energy Dispersive Spectroscopy (SEM-EDS) and Focused Ion Beam - Scanning Electron Microscopy (FIB)-SEM. Complementary, secondary MFI in pyroxenites from COC were also investigated. MFI hosted in eclogite and granulites occur along growth zones or in 3D clusters in garnet porphyroblasts suggesting a primary origin at high-pressure (HP) metamorphic conditions. The mineral assemblage of MFI is mainly composed of Fe-Mg-Ca-carbonates and phyllosilicates ± graphite ± quartz ± corundum ± pyrite ± apatite ± rutile and a fluid phase composed of nitrogen ± methane ± carbon-dioxide. The mineral proportions vary among the lithologies. Dominant carbonates and hydrous silicates are interpreted as step-daughter minerals (crystals formed in the MFI after entrapment as a result of fluid–host interaction), whereas apatite, quartz and rutile are considered in part as accidentally trapped minerals since they also occur as crystal inclusions together with MFI in each rock type. Quartz and corundum occur together in MFI in ultramafic granulite and are regarded as step-daughter minerals in this lithology. These observations suggest that the MFI are products of post-entrapment reactions of a homogeneous COHN fluid system with the host mineral. Thermodynamic calculations in the CaFMAS-COHN system confirmed that bulk composition of the MFI in eclogite is similar to the host garnet+COHN composition except for a potential lost of H_2O. Carbonation and hydration reaction between the host (i.e. garnet or pyroxene) and the fluid inclusion results in the consumption of all CO_2 and part of the H_2O from the fluid phase producing Ca-Fe-Mg-carbonates and hydrous step-daughter minerals, mostly pyrophyllite and chlorite. Nitrogen content of the originally

trapped COHN fluid in eclogite was estimated to have a maximum value of 10 mol% at peak HP conditions and 30–40 mol% at retrograde conditions that is within the range of the observed MFI in the residual fluid (13–68 mol%). Pseudosection modelling confirmed the stability of the phase assemblage in the MFI in a specific low-pressure, low-temperature stability field (between 300°C and 400°C at pressures < 1 GPa), caused by H_2O- and CO_2-consuming reactions possibly in a single step. Our findings indicate that such processes in the exhuming HP units may play a role in global nitrogen and carbon cycling as well as potentially contributing to nitrogen and methane supply to subsurface–surface environments during devolatilization in the forearc regions of convergent plate margins.

KEYWORDS
Cabo Ortegal Complex, multiphase fluid inclusions, nitrogen cycling, subduction fluid, Raman imaging

1 | INTRODUCTION

Subduction zone fluids, derived from dehydration reactions in the downgoing slab, are responsible for large-scale mass transfer at convergent plate margins as well as for inducing metasomatism and partial melting in the mantle wedge. Previous studies (Bebout, 2007; Hermann et al., 2006; Kessel et al., 2005; Manning, 2004; Poli & Schmidt, 2002) concluded that element transport from the subducted slab to the overlying mantle wedge is mediated mostly by hydrous fluids, playing an important role (1) during metamorphic processes at high-pressure (HP)-ultrahigh-pressure (UHP) conditions and (2) in volatile cycling between near-surface geospheres and deep Earth reservoirs. Exhumed HP-UHP metamorphic rocks, as primary representatives from deep parts of subduction zones, yield direct records on subduction fluids, which can be trapped as fluid/melt inclusions (Carswell & Compagnoni, 2003; Frezzotti & Ferrando, 2007, 2015; Scambelluri & Philippot, 2001; Touret, 2001). Comprehensive data on fluid inclusions, observed in HP and UHP rocks, show a wide variety of phase assemblages and composition, including (1) inclusions with saline aqueous and/or non-polar gaseous fluids which vary in terms of solutes (e.g. Philippot & Selverstone, 1991; Scambelluri & Philippot, 2001), (2) multiphase solid inclusions (MSI) representing remnants of supercritical fluids (e.g. Ferrando et al., 2005; Frezzotti & Ferrando, 2007; Maffeis et al., 2021; Ni et al., 2017) and (3) inclusions derived from hydrous melts (e.g. Korsakov & Hermann, 2006). For a comprehensive summary, see Hermann et al. (2006, 2013) and Frezzotti and Ferrando (2015).

It is widely recognized that H_2O is the most abundant volatile component in subduction zones, characterized by enhanced mineral solubility under supercritical conditions and especially at near the second end-critical point (Hermann et al., 2006; Dolejš & Manning, 2010; Manning, 2004; Newton & Manning, 2010). Moreover, CO_2, CH_4 and N_2 can also be frequent constituents (e.g. Frezzotti & Ferrando, 2015; Manning, 2004; Scambelluri & Philippot, 2001; Tiraboschi et al., 2018). Fluid inclusion and thermodynamic modelling also suggest that eclogites have been equilibrated with H_2O-dominated fluids (Andersen et al., 1993; Holland, 1979; Jamtveit et al., 1990). However, several studies showed that mixed H_2O-CO_2-N_2-CH_4 ± solids inclusion and brines are also present in eclogite facies rocks (e.g. Andersen et al., 1989; Fu et al., 2003; Scambelluri & Philippot, 2001). Slab-derived carbonic fluids in subduction zones trigger chemical interaction with the host-rock assemblage, resulting the formation of extensive carbonate-dominated veins even in carbonate-free rocks, together with carbonation of serpentinites and production of ophicarbonates, evidenced at different stages during exhumation (Menzel et al., 2018; Peng et al., 2020; Piccoli et al., 2016; Scambelluri et al., 2016).

Nitrogen species preserved in rocks provide a direct record on past geochemical nitrogen cycling. The balance of its input/output during global recycling processes has been widely investigated, mostly by isotopic studies (e.g. Busigny & Bebout, 2013; Halama et al., 2012). Volatile recycling by conveying subducted ultramafic units evolved along the slab-mantle interface provide important contributions to the deep Earth diamond genesis (N may substitute C in concentrations up to 11,000 ppm) (Cannaò et al., 2020; Cartigny et al., 2001; Cartigny & Marty, 2013; Halama et al., 2012). Studying the nature of nitrogen during its transport and retention into deep

reservoirs together with degassing at convergent margins is of great importance for our understanding of the planetary atmospheric evolution (Mikhail & Sverjensky, 2014). Although subduction zone cycling defines nitrogen transfer together with non-radiogenic noble gas isotopes as the major exchange between near-surface geospheres and deep Earth reservoirs (Kendrick et al., 2011, 2018), the mechanism governing the enrichment of nitrogen and explanation of its abundance in forearc regions of accretionary subduction complexes is poorly understood.

The Cabo Ortegal Complex (COC) in NW Spain is formed by metamorphic rocks from a former subduction zone and is a well-studied locality in terms of petrologic, geochemical and structural aspects (e.g. Ábalos et al., 1996, 2003; Albert et al., 2015; Gil Ibarguchi et al., 1990, 1999; Henry et al., 2017; Llana-Fúnez & Brown, 2012; Marcos et al., 2002; Ordóñez Casado et al., 2001; Puelles et al., 2005, 2009; Tilhac et al., 2016, 2017). By contrast, the fluids, which were present during different stages of its pressure and temperature (P–T) evolution, are poorly constrained. In this study, we characterize for the first time and then discuss the significance of multiphase fluid inclusions (MFI) preserved in metamorphic rocks from the COC. We propose a possible evolution of such trapped fluids during the retrograde exhumation path supported by thermodynamic modelling. The passive enrichment of nitrogen during post-entrapment carbonation and hydration processes with their hosts observed in MFI provides new constraints to better understand the preservation of subduction fluids and nitrogen cycling in subduction zones.

2 | GEOLOGICAL BACKGROUND

The COC, located in the northwestern edge of the Iberian Peninsula, forms the upper structural unit of the Allochtonous Complexes exposed in the Iberian Massif (Figure 1) (Ábalos et al., 2003; Albert et al., 2015; Martínez Catalán et al., 2009). These complexes belong to the Variscan belt of Europe and are interpreted as fragments of continental and oceanic lithosphere, which were involved in a Devonian subduction-exhumation cycle (Puelles et al., 2005). The rocks of the COC record a multistage tectonothermal history as a result of prograde and retrograde metamorphism. The structural units, separated by ductile thrust contacts, are thought to have been amalgamated and undergone HP deformation in deep tectonic realms of a Variscan subduction/collision orogenic channel (Ábalos et al., 2003; Puelles et al., 2005). The studied area comprises high-pressure and high-temperature (HP-HT) ultramafic massifs associated with eclogites, granulites, orthogneisses, paragneisses and metagabbros (Figure 1) (Arenas, 1991;

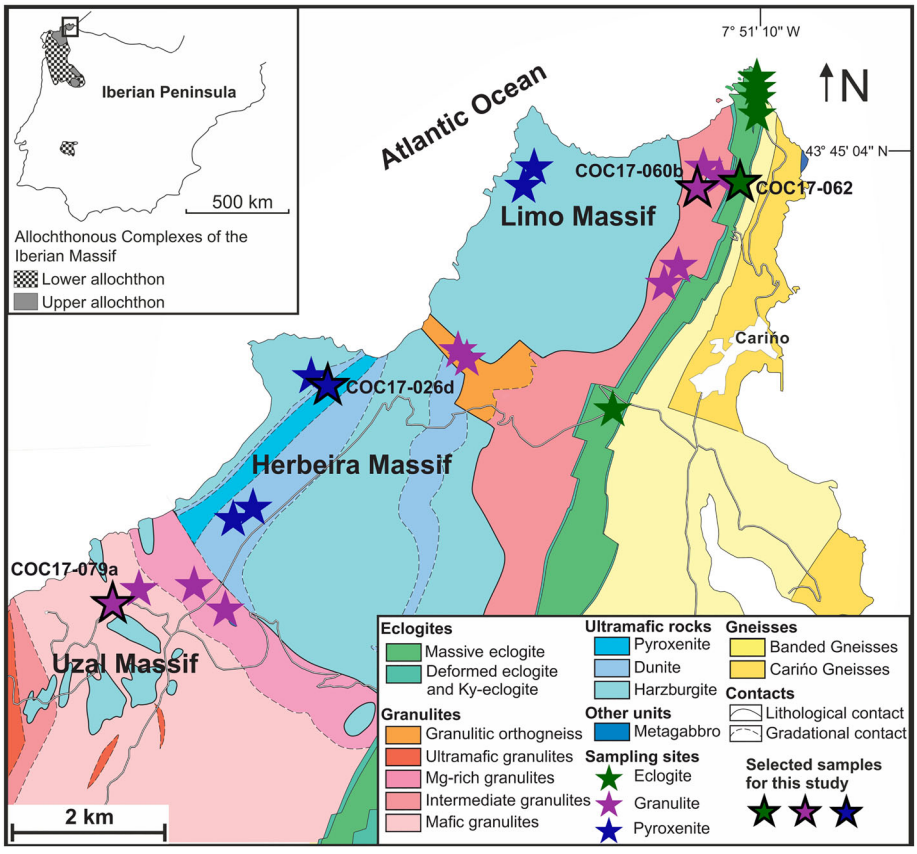

FIGURE 1 Simplified geological map of the Cabo Ortegal Complex (COC) modified after Ábalos et al. (2010). Locations of the sampled and selected eclogites, granulites and pyroxenites are indicated with colored stars; sample names are indicated for selected samples in this study [Colour figure can be viewed at wileyonlinelibrary.com]

Den Tex, 1961; Gil Ibarguchi et al., 1990, 1999; Vogel, 1967). The origin of the main HP metamorphic units is rather well constrained: subcontinental lithospheric mantle for the peridotites and pyroxenites, middle to upper crustal volcanic arc for the granulites, N-MORB for the eclogites and shallow crustal volcanosedimentary sequences for the gneisses (Ábalos et al., 2003; Santos Zalduegui et al., 2002). Pyroxenites are thought to have been formed by melt–peridotite interaction in a suprasubduction setting around 459–515 Ma ago based on Rb-Sr and Sm-Nd dating (Santos Zalduegui et al., 2002; Tilhac et al., 2017). The following PT conditions of peak metamorphism have been acquired for the main units of the COC: ultramafics (1.6–1.8 GPa, 780–800°C), eclogite (1.8–2.2 GPa, 700–800°C), granulite (1.4–1.7 GPa, 740–835°C) and gneiss (approximately 1.5 GPa, 700°C) (Ábalos et al., 2003; Gil Ibarguchi et al., 1990; Mendia, 2000; Puelles et al., 2005; Tilhac et al., 2016, 2017). The age of peak metamorphism (approximately 382–389 Ma U–Pb on titanite and zircon; SHRIMP U–Pb on zircon and internal Sm-Nd isochrons on Cpx–Grt–whole-rock), recorded in eclogites and granulites, corresponds to the formation and accretion of the HP sheets of the units of the COC at sub-Moho depths (Ábalos et al., 2003; Ordóñez Casado et al., 2001; Peucat et al., 1990; Santos Zalduegui et al., 2002). A single PT-loop has been assigned for the metamorphic evolution of granulites as well during Variscan subduction, as being a part of a coherent ensemble together with other HP rocks in the COC during exhumation (Puelles et al., 2005). Simultaneously, ultramafic rocks have undergone eclogite facies metamorphism and deformation. This was followed by percolation of hydrous fluids causing metamorphic amphibolization of pyroxenites and hydration of their host peridotites (Tilhac et al., 2017). The presence of a low-viscosity subduction channel, active between ca. 395 and 365 Ma, and fast exhumation of HP units with a rate comparable to plate motions has been inferred for the serpentinite-matrix mélange rocks, which occur in the lowest structural position of the COC (Ábalos et al., 2003, 2010; Novo-Fernández et al., 2016).

The eclogitic unit of the COC forms one of the largest known continuous eclogite outcrops with a ridge 100–700 m thick and 17 km long in the direction N-NE to S-SW (Ábalos, 1997). Detailed petrographic, mineralogical, geochemical, structural and thermobarometric data of eclogites are provided by Ábalos et al. (2010), Gil Ibarguchi et al. (1990), Mendia (2000) and Vogel (1967). Based on the consistency of isotopic and geochemical characteristics, the whole eclogite massif has an oceanic crustal origin (Bernard-Griffiths et al., 1985; Peucat et al., 1990), representing different stages of N-MORB tholeiitic series with variable degrees of differentiation (Ábalos et al., 2010; Mendia, 2000). Consequently, besides the most abundant variety, termed as N-MORB or massive eclogite, kyanite-rich deformed and ferrotitaniferous eclogites can be further distinguished (Gil Ibarguchi et al., 1990; Mendia, 2000).

Granulite facies rocks of the COC comprise various lithostratigraphic units: granulitic orthogneisses, ultramafic, Mg-rich mafic, intermediate and common mafic granulites, although the protolith of each subtype of granulite is not fully constrained (Gil Ibarguchi et al., 1990; Puelles et al., 2005; Vogel, 1967).

Ultramafic massifs (Herbeira, Limo and Uzal), structurally constituting the uppermost section of the COC, are composed dominantly of serpentinized spinel-bearing harzburgite with abundant layers of spinel-bearing and locally garnet-bearing pyroxenites and websterites, which are interlayered with chromian spinel- and platinum-group mineral-bearing dunite, described comprehensively by Gil Ibarguchi et al. (1999), Girardeau and Gil Ibarguchi (1991), Santos Zalduegui et al. (2002), Tilhac et al. (2016, 2017, 2020) and Vogel (1967). In addition to eclogite and granulites, pyroxenites were also considered in this study and they correspond to *Type-3* pyroxenites classified by Tilhac et al. (2016), showing high degree of amphibolization possibly caused by deformation and percolation of hydrous fluids during retrograde processes. Clinopyroxene, as major constituent of these pyroxenites, is diopside with low contents of Cr, Ti and Na (Girardeau & Gil Ibarguchi, 1991).

3 | PETROLOGY OF THE STUDIED HP ROCKS AND SAMPLING

The eclogites are medium to coarse-grained rocks, characterized by a slight-moderate foliation. They are mainly composed of garnet, omphacite, quartz, zoisite, rutile and zircon, whereas secondary diopsidic pyroxene and amphibole (hornblende) form symplectitic intergrowths with plagioclase as a replacement of omphacite and garnet (Gil Ibarguchi et al., 1990; Peucat et al., 1990; Vogel, 1967). Garnet forms euhedral to subhedral millimeter- to centimeter-sized crystals with abundant mineral inclusions (quartz, rutile, zoisite and amphibole) in the core and inner zones (Gil Ibarguchi et al., 1990). Needle-shaped rutile inclusions in garnet were considered as outlines of a former igneous phase (clinopyroxene or titanite) by Gil Ibarguchi et al. (1990) and Vogel (1967). Garnet porphyroblasts are characterized by almandine-pyrope-grossular solid solutions ($Alm_{30-52}Prp_{25-40}Sps_{0-2}Grs_{20-25}$,) and display a weak chemical zoning with a decrease of Ca together with a slight Fe and Mg increase from core to rims, indicating

prograde zonation (Gil Ibarguchi et al., 1990; Mendia, 2000).

Mineral assemblages in textural equilibrium in ultramafic to intermediate granulites contain garnet, clinopyroxene and plagioclase with different amounts of zoisite/clinozoisite, kyanite, quartz, scapolite, rutile, ilmenite and zircon depending on the lithotype. Locally, ultramafic granulites may exhibit a monomineralic composition made up almost exclusively by garnet. Retrograde assemblages comprise hornblende ± actinolite, biotite, chlorite, zoisite and plagioclase-clinopyroxene symplectite. Garnet exhibits a weak compositional variability between granulite subtypes ($Alm_{43–58}Grs_{7–29}Prp_{11–28}And_{1–9}Sps_{1–3}$ for intermediate and $Alm_{38–55}Grs_{17–32}Prp_{15–34}And_{2–13}Sps_{1–4}$ for ultramafic granulites), although they show no significant trends within samples or only locally weak normal zoning from core to rim, which is explained by compositional homogenization during peak HP granulite facies metamorphism (Puelles et al., 2005). Garnet contains rutile, quartz or zircon inclusions sometimes with a concentric arrangement, which is likely related to different growth stages (Beranoaguirre et al., 2020; Puelles et al., 2005).

During systematic sampling, we collected 38 samples (18 eclogites and 20 granulites) from 17 outcrops (Figure 1). This study focuses on rock samples from three outcrops (one eclogite, one ultramafic and one intermediate granulite) being the most suitable for fluid inclusion study (Figure 1). Additional 18 samples of pyroxenites from 6 outcrops have been collected from both Herbeira and Limo Massifs of the COC.

4 | ANALYTICAL METHODS

From the selected eclogite, granulite and pyroxenite samples from the COC, 60–100 μm thick and 30 μm doubly polished thin sections have been prepared. Fluid inclusion petrography was carried out in the Lithosphere Fluid Research Lab, Eötvös University, Budapest, using a Nikon OptiPhot2 optical microscope equipped with a Nikon CoolPix DS-Fi1 camera. The details on the analytical methods concerning SEM-EDS, Raman spectroscopy and FIB-SEM analyses are reported in supporting information (Appendix S1). The applied procedure to calculate the bulk MFI composition is provided in detail in Appendix S2 and Tables S3–S10. Mineral abbreviations are after Whitney and Evans (2010), except for specific and fictive endmembers of solid solutions (in Tables 3, S12 and S14) from Holland and Powell (2011) database and related works as used by Perple_X.

Phase equilibria and electrolyte fluid speciation, using bulk compositions of MFI from eclogite and ultramafic granulite, were computed by Gibbs energy minimization using the PerpleX algorithm (Connolly, 1990, 2009; Connolly & Galvez, 2018). The endmember thermodynamic dataset and activity-composition models used are given in Appendix S1. Thermodynamic modelling focuses on the MFI bulk compositions of the eclogite and ultramafic granulite as having the most robust data from these samples (Table 2). Pseudosections were computed assuming a molecular fluid model, whereas electrolytic model, using the lagged minimization algorithm, was calculated at the two representative HP-HT and low-pressure–low-temperature (LP-LT) conditions for comparison (Figures 10 and S5 and Tables 3 and S12) and when estimating the potential original fluid in equilibrium with the bulk eclogite composition (Figure S1 and Tables S14 and S15). Forward thermodynamic modelling has been performed in the CaFMAS-COHN system using elements as thermodynamic system components (Ca-Fe-Mg-Al-Si-C-O_2-H_2-N_2) to investigate solid phase relations with a COHN fluid. Fluid saturation conditions were not imposed during the computation; for further details see Appendix S1. The potential original composition of the fluid in equilibrium with the eclogite—using bulk rock data from by Gil Ibarguchi et al. (1990), sample 97—was estimated using both molecular and electrolyte fluid speciation (details in Appendix S3).

5 | RESULTS

5.1 | Petrography

The studied eclogite (COC17-062) is coarse-grained, moderately sheared and mostly made up by garnet and omphacite (Figure 2a). In minor amounts, quartz, zoisite and rutile together with retrograde amphibole, chlorite and plagioclase-diopsidic pyroxene symplectite are also present. Garnet porphyroblasts are found as euhedral to subhedral 0.5–10 mm crystals, whereas omphacite with a size of 100–800 μm is usually anhedral, slightly elongated and commonly characterized by plagioclase-diopsidic pyroxene symplectite on the edges. Garnet crystals exhibit a characteristic zoning with respect to color and occurrence of inclusions. The following crystal zones were identified as follows: (1) core (zone 1) shows a dark pink color with abundant oriented needle-shape rutile, a few zircon and apatite inclusions, and (2) mantle (zone 2) exhibits light pink color and can be identified as a zone enriched in quartz and rutile inclusions, and the rim of garnet (zone 3) is nearly colorless and contains very few or no crystal inclusions (Figure 3a). Primary fluid inclusions occur within the growth zone 2 of garnet (Figure 3b).

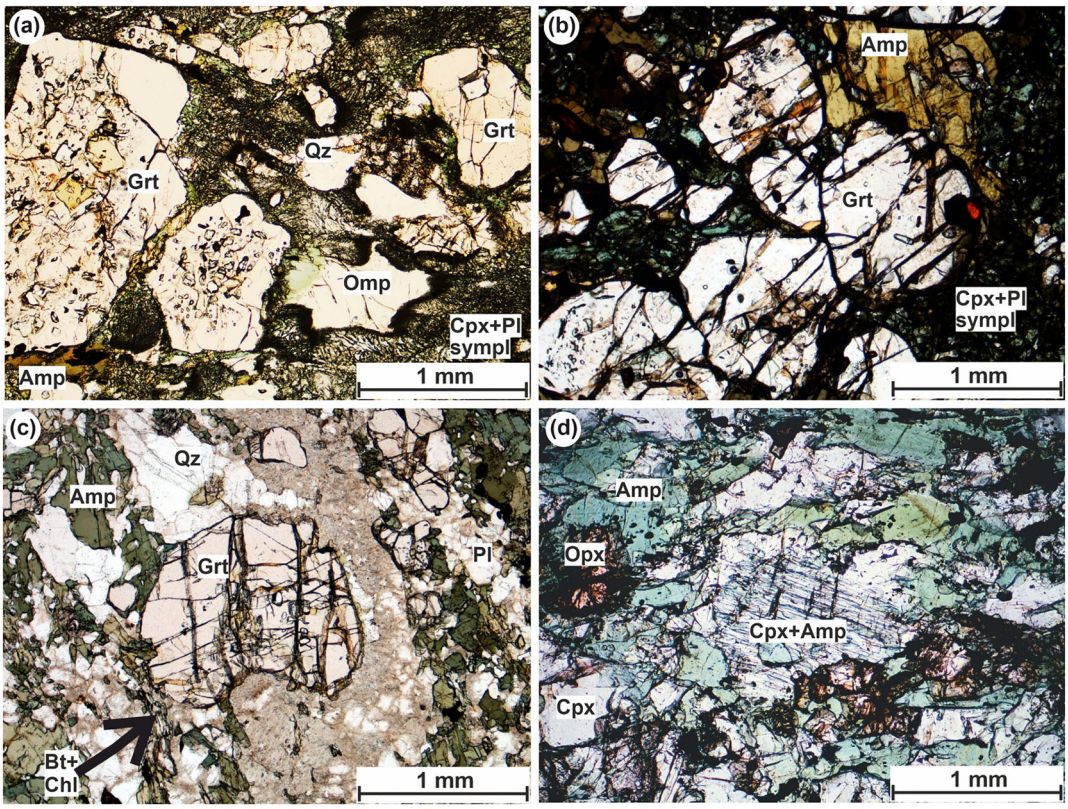

FIGURE 2 Photomicrographs showing characteristic petrographic features of the studied rock types from the Cabo Ortegal Complex (COC). (a) Coarse grained eclogite (COC17-062) showing typical texture of rock-forming minerals such as garnet, omphacite and amphibole ± quartz and clinopyroxene-plagioclase symplectite (Cpx-Pl sympl); (b) ultramafic granulite (COC17-079a) showing euhedral garnet, anhedral clinopyroxene and amphibole together plagioclase+clinopyroxene symplectite as major constituents; (c) intermediate granulite (COC17-060b) consisting of subhedral and altered garnet forming a porphyronematoblastic texture with plagioclase, amphibole, biotite and chlorite; (d) pyroxenite (COC17-026d) dominated by highly amphibolized clinopyroxene and orthopyroxene. Photomicrographs were taken under plane polarized light [Colour figure can be viewed at wileyonlinelibrary.com]

Among the various granulite subtypes in the COC, ultramafic and intermediate granulites have been selected for this study as containing fluid inclusions in significant quantities. The studied ultramafic granulite (COC17-079a) is a slightly sheared granoblastic rock, which is mostly made up by euhedral garnet (up to 1 mm in diameter) and anhedral clinopyroxene, without plagioclase (Figure 2b). The intermediate granulite (COC17-060b) is foliated and is strongly retrogressed, being dominated by plagioclase, garnet and partially to completely amphibolized clinopyroxene (Figure 2c). Subhedral garnet crystals (0.1–1 mm in size) have a shape-preferred orientation forming porphyronematoblastic texture with plagioclase, clinopyroxene, amphibole, zoisite, quartz, rutile, zircon and opaque minerals. The retrograde assemblage in both types consists of hornblende ± actinolite, biotite, chlorite, zoisite and plagioclase-clinopyroxene symplectite. Garnet porphyroblasts in both granulite types have several cracks and have subhedral to anhedral grain boundaries indicating breakdown reactions. Despite this, core and inner zones are commonly undisturbed and contain primary MFI commonly together with crystal inclusions such as quartz, rutile and zircon.

The selected pyroxenite sample (COC17-026d) has a medium to coarse grained porphyroclastic texture with a slight foliation. It mostly consists of clinopyroxene with minor amounts of amphibole, orthopyroxene, olivine, spinel and serpentine (Figure 2d). Clinopyroxene porphyroclasts, commonly partially replaced by amphibole along cleavages, are 0.5–5 mm in size, whereas serpentine associated with veins are widespread and overprint the development of each rock-forming mineral (Figure 2d). Clinopyroxene, showing a lower degree of serpentinization, hosts secondary fluid inclusions. Graphite has not been identified in the rock matrix of any of the rock types.

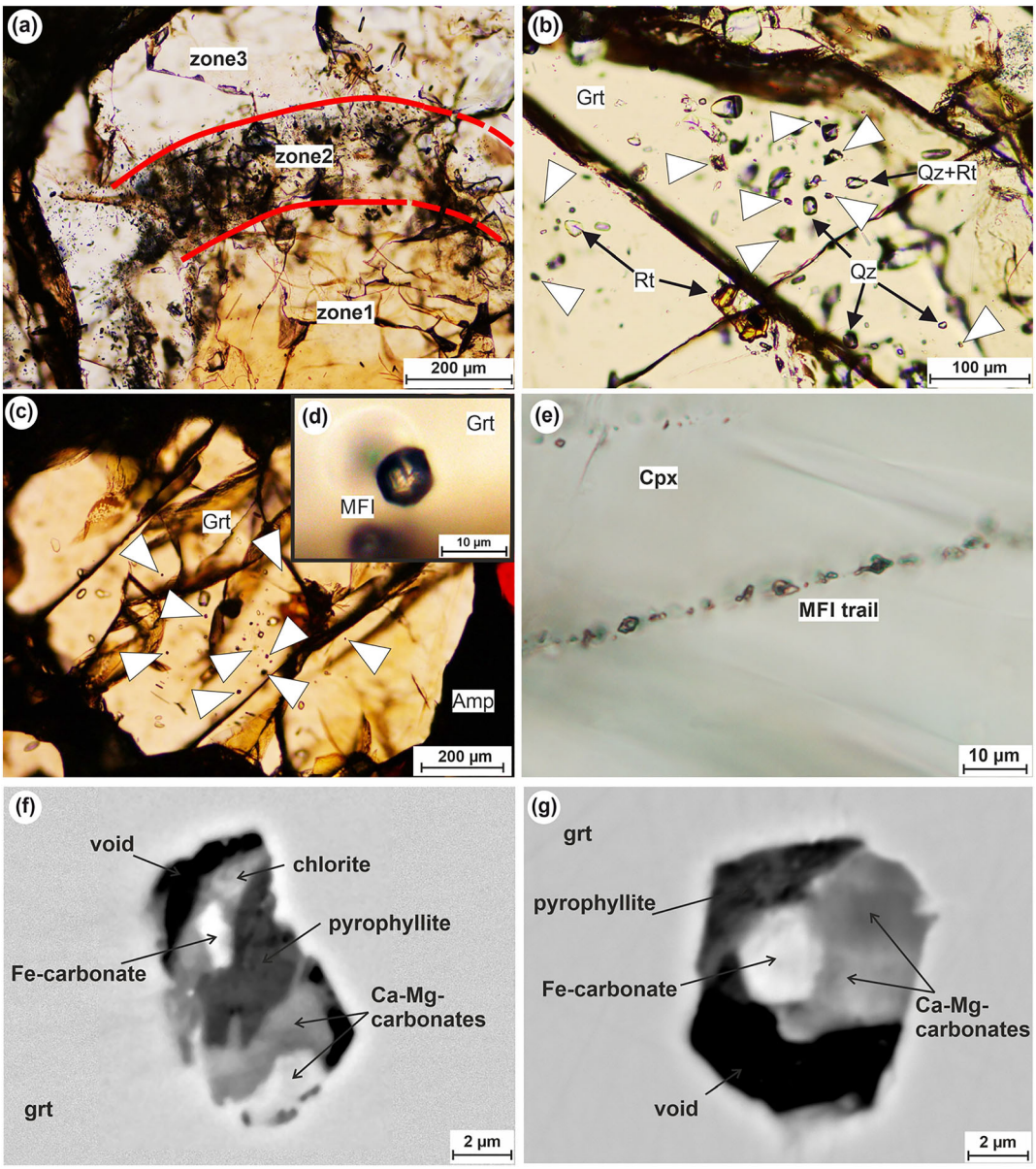

FIGURE 3 Photomicrographs showing petrographic characteristics of multiphase fluid inclusions (MFI) in garnets of the studied rocks. (a) Characteristic zoning pattern of garnet in eclogite showing the occurrence of MFI in zone2; (b) randomly distributed primary MFI together with quartz and rutile inclusions along the growth zone (zone 2) of garnet in eclogite; (c) primary MFI appearing in 3D cluster in ultramafic granulite; (d) a close-up view of primary negative crystal-shaped MFI made up by micron-submicron-sized aggregates of solid phases in ultramafic granulite; (e) secondary MFI occurring along a healed fracture in clinopyroxene of pyroxenites; (f, g) SEM-EDS images of exposed MFI of eclogite (f) and intermediate granulite (g) showing intergrowth of Ca-Fe-Mg-carbonates and phyllosilicates (pyrophyllite and chlorite) in MFI. Note that proper structural identification of the phases has been carried out using Raman spectroscopy. White arrows point to primary MFI. Photomicrographs (a)–(e) were taken under plane polarized light [Colour figure can be viewed at wileyonlinelibrary.com]

5.2 | Fluid inclusion petrography and SEM-EDS analyses

MFI in eclogite are described as primary inclusions as they appear only within the zone 2 of garnet (Figure 3a) together with rutile and quartz inclusions (Figure 3b). MFI have irregular shape with size between 5 and 40 µm, whereas inclusions below 8–10 µm are polygonal (Figure 8a), approaching negative crystal shapes, and those above 15–20 µm commonly indicate partial or complete decrepitation (Figure 3b).

Similar to the eclogite, a primary origin of MFI in granulites is suggested by their distribution in 3D clusters in the dark pink core and inner zones of garnet

(Figure 3c). Rutile, quartz and zircon inclusions are commonly associated with these 3D clusters. MFI in granulites are smaller in size than those in eclogite (3–20 μm) and have negative crystal shapes (Figure 3d), whereas bigger inclusions are partially or fully decrepitated indicated by spherical-irregular decrepitation halos and comprising only solid phases.

Petrography and SEM-EDS analyses of exposed inclusions showed that MFI in both rock types are built up by aggregates of multiple micron-submicron-sized solid phases (Figure 3f,g); some of them (i.e. carbonates) are characterized by high birefringence under cross-polarized light. Carbonates, phyllosilicates, quartz and corundum have been detected in exposed MFI (Figure 3f,g). Carbonates consist of several minerals based on the variation in the ratio of Fe, Ca and Mg within a single multiphase fluid inclusion in each rock type (Table S2). Phyllosilicates including chlorite (Fe-Al-silicate) have been observed exclusively in MFI from eclogite, whereas pyrophyllite (Al-silicate) occurs in eclogite and both type of granulites (Table 2). Quartz and corundum are also present in MFI of ultramafic granulite.

In the investigated pyroxenite, secondary inclusions occur along healed fractures of clinopyroxene. The trails of fluid inclusions crosscut the orientation of amphibole lamellae in clinoproxene, typically running out to grain boundaries. The inclusions are smaller than 5 μm and show irregular and elongated shape (Figure 3e). Optical microscopy revealed the presence of at least one tiny (up to 1–2 μm) solid mineral indicated by high birefringence.

5.3 | Raman spectroscopy

Raman spectroscopy revealed that MFI in eclogite and granulites show similar but distinct assemblages in terms of solids in the MFI. The solid phase assemblage in MFI in eclogite is Fe-Mg-Ca-carbonates + pyrophyllite + Fe-chlorite ± quartz ± graphite ± corundum ± sulfide ± apatite ± rutile, in ultramafic granulite Fe-Mg-Ca-carbonates + pyrophyllite + quartz + corundum ± graphite ± sulfide ± apatite ± rutile, whereas in intermediate granulite it comprises Fe-Mg-Ca-carbonates + pyrophyllite + margarite ± quartz ± corundum ± graphite ± sulfide ± apatite ± rutile. These minerals show highly similar characteristic in terms of Raman spectra; therefore, their properties are discussed together with indications of differences as well. Representative Raman spectra of each phase are provided in Figure 4. Carbonates and phyllosilicates, dominated by pyrophyllite (262, 195, 705, 216, 113, 814 and 3,671 cm^{-1}) are always present; however, Fe-chlorite occurs only in MFI from the investigated eclogite, whereas margarite occurs in the MFI of investigated intermediate granulite. Identification of Raman bands of phyllosilicates, like pyrophyllite, Fe-rich chlorite and margarite was carried out using the data from Wang et al. (2015). Margarite is present exclusively in MFI from intermediate granulite with a strong spatial overlap with pyrophyllite or in small amounts within it. The characteristic feature of margarite is a low intensity band appearing around 393 cm^{-1}, together with an additional band at 3,633 cm^{-1} in addition to the OH^- vibration mode of pyrophyllite (3,671 cm^{-1}) (Figure 4). Chlorite (main Raman bands at 336, 471, 554 and 661 and a triplet OH peak at 3,450, 357 and 3,625 cm^{-1}) is associated with pyrophyllite. Raman spectra of carbonates (Figure 4) indicate the presence of at least two types of Ca-Fe-Mg-carbonates with non-end-member mineral chemistry (Gillet et al., 1993; Rutt & Nicola, 1974). Calibrations for defining compositions from Raman spectroscopy proposed by Boulard et al. (2012) and Rividi et al. (2010) indicate a continuous shift of Raman bands between the two end-members of solid solutions (calcite-magnesite-siderite-rhodochrosite and dolomite-ankerite-kutnahorite series). Therefore, as a first approximation, they can be considered as siderite (1,087, 292, 187, 730 and 1,732 cm^{-1}) and ankerite (1,093, 283, 168, 722, 1,741 and 1,438 cm^{-1}) as the best fitting mineral species. In small inclusions (below 8–10 μm), carbonates are difficult to distinguish from each other, because they are finely intergrown, based on the nearly continuous transition of characteristic Raman bands. Even for larger inclusions, their spatial distribution shows a broad overlap. To make Raman image analyses and further calculations unambiguous, carbonates will be considered hereinafter together.

Corundum and quartz occur together in MFI of ultramafic granulite. Corundum was also confirmed in MFI of eclogite in a few cases. Apatite, quartz and rutile occur occassionally in MFI and commonly as individual crystal inclusions in the host garnet. Raman bands with low intensities at 340, 372 and 424 cm^{-1} indicate the presence of pyrite observed as small spots at the wall of some of the inclusions. Graphite, with intense Raman bands at 1,341 and 1,605 cm^{-1}, occurs as few micron-submicron-sized spots distributed together with the fluid phase.

Solid phases in secondary MFI in pyroxenites have also been identified as carbonate (calcite: 1,086, 281, 158 and 712 cm^{-1}) and phyllosilicate (talc: 190, 114, 3,675 and 3,661 cm^{-1}) (Figure S2). In addition, these inclusions are volumetrically dominated by fluid phases such as nitrogen and to a lesser extent methane, so they can be also regarded as MFI.

Generally, MFI in all rock types contain N_2 (2,327 cm^{-1}) as the dominant fluid component, together with various amounts of CH_4 (2,913 cm^{-1}) and CO_2

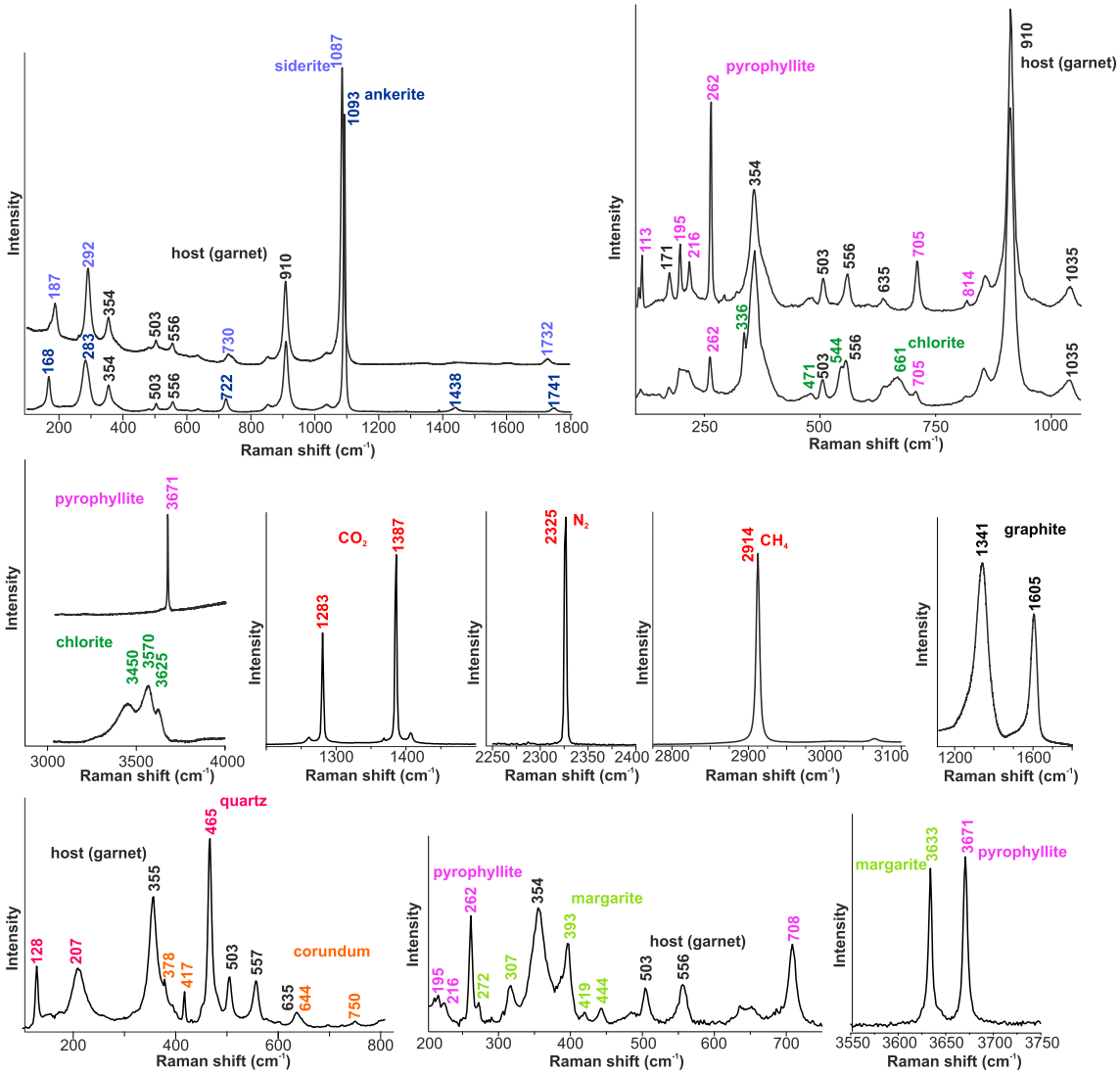

FIGURE 4 Representative Raman spectra of solid and fluid phases in garnet-hosted multiphase fluid inclusions (MFI) in the studied eclogites and granulites. Chlorite is present only in MFI of eclogites, whereas quartz and corundum occur together in MFI of ultramafic granulites, and margarite is found only in MFI of intermediate granulites. Graphite occurs occasionally in MFI of each rock type (most often in eclogites) [Colour figure can be viewed at wileyonlinelibrary.com]

(1,281 and 1,386 cm^{-1}). According to the evaluation of integrated areas of Raman spectra, fluid compositions in eclogite vary as follows N_2: 13–68 mol%, CH_4: 21–87 mol % and CO_2: 0–40 mol% (Table 1). The fluid phase of MFI in granulites is dominated by carbon-dioxide (ultramafic granulite: CO_2: 88–96 mol% and N_2: 4–12 mol%, intermediate granulite: CO_2: 71–88 mol%, N_2: 12–29 mol% and CH_4: 0–4 mol%) (Table 1). The fluid phase in MFI of pyroxenites is extremely enriched in nitrogen: N_2: 75–95 mol%, CH_4: 5–25 mol% (Table 1). A distribution diagram showing fluid compositions of the measured individual MFI in each studied rock type is shown in Figure 5 (for the data, see Table S1). The relative amount of these fluids shows a small variation (± 5–10 mol%) in a single inclusion.

Approximate modal proportions of dominant solid and fluid phases are calculated based on pixel counts of each phase on Raman images (Figure 6), indicated in Table 2. MFI are comprised by carbonates with 22–45 area % in eclogite and 21–38 area % in granulite. Pyrophyllite is present in all MFI from eclogite with 18–31 area %, 7–18 area % in ultramafic and 20–31 area % in MFI of intermediate granulite. Such calculation within 30 unexposed MFI in eclogite, nine in ultramafic and six in intermediate granulite reveal nearly uniform volume ratios of the phases, making a reliable base of FIB-SEM

TABLE 1 Relative proportions (in mol%) of fluid phases determined by Raman spectroscopy inside unexposed MFI in the studied rocks

	Primary MFI in eclogites ($n = 14$)			Primary MFI in ultramafic granulites ($n = 16$)			Primary MFI in intermediate granulites ($n = 15$)			Secondary MFI in pyroxenites ($n = 8$)		
	min	max	aver	min	max	aver	min	max	aver	min	max	aver
N_2	13	68	43	4	12	6	12	29	21	75	95	84
CH_4	21	87	52	-	-	-	0	4	<1	5	25	16
CO_2	0	40	6	88	96	94	71	88	79	-	-	-

Note: The complete dataset is presented in Figure 5. 'aver' refers to the average value for fluid composition in each rock type.
Abbreviation: max, maximum; MFI, multiphase fluid inclusion; min, minimum; n, number of analyses.

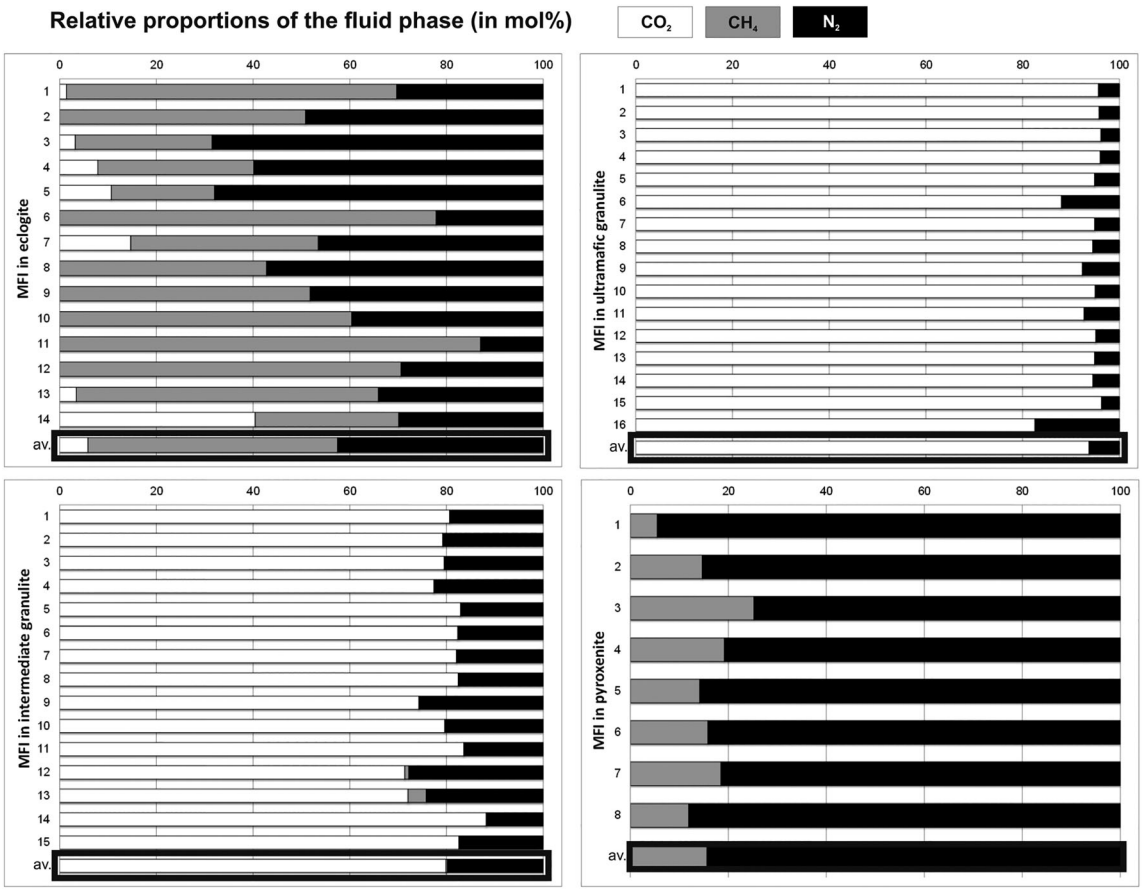

FIGURE 5 Distribution diagrams showing the relative proportion of components in the fluid phase (in mol%). Abbreviation 'av.' refers to the average of measurements in each rock type

serial sectioning on selected representative MFI from each eclogite and granulite sample (Table 2).

5.4 | Gradual exposure of MFI with FIB-SEM

Considering data of MFI obtained with Raman imaging, FIB-SEM analyes were carried out on four representative MFI (two from eclogite, one from intermediate and one from ultramafic granulite). In accordance with Raman imaging on the same MFI, carbonates, phyllosilicates, corundum, quartz, graphite and pyrite were observed in tight intergrowths (Figure 7a,c,d). Each of them shows direct contact to the host garnet. Chemical variability in Ca, Fe and Mg of euhedral carbonates is visible on back-scattered electron images (Figure 7a,c,d). Two different types of carbonates can be distinguished on BSE images: (i) Ca-rich Fe-Mg-bearing ankerite and (ii) Fe-rich Ca-Mg-bearing for siderite, with an estimated ratio of similar as it was inferred based on Raman spectra (Figure 4). Although, to make further calculations straightforward, carbonates are treated together with representative compositions with respect to their estimated relative volume

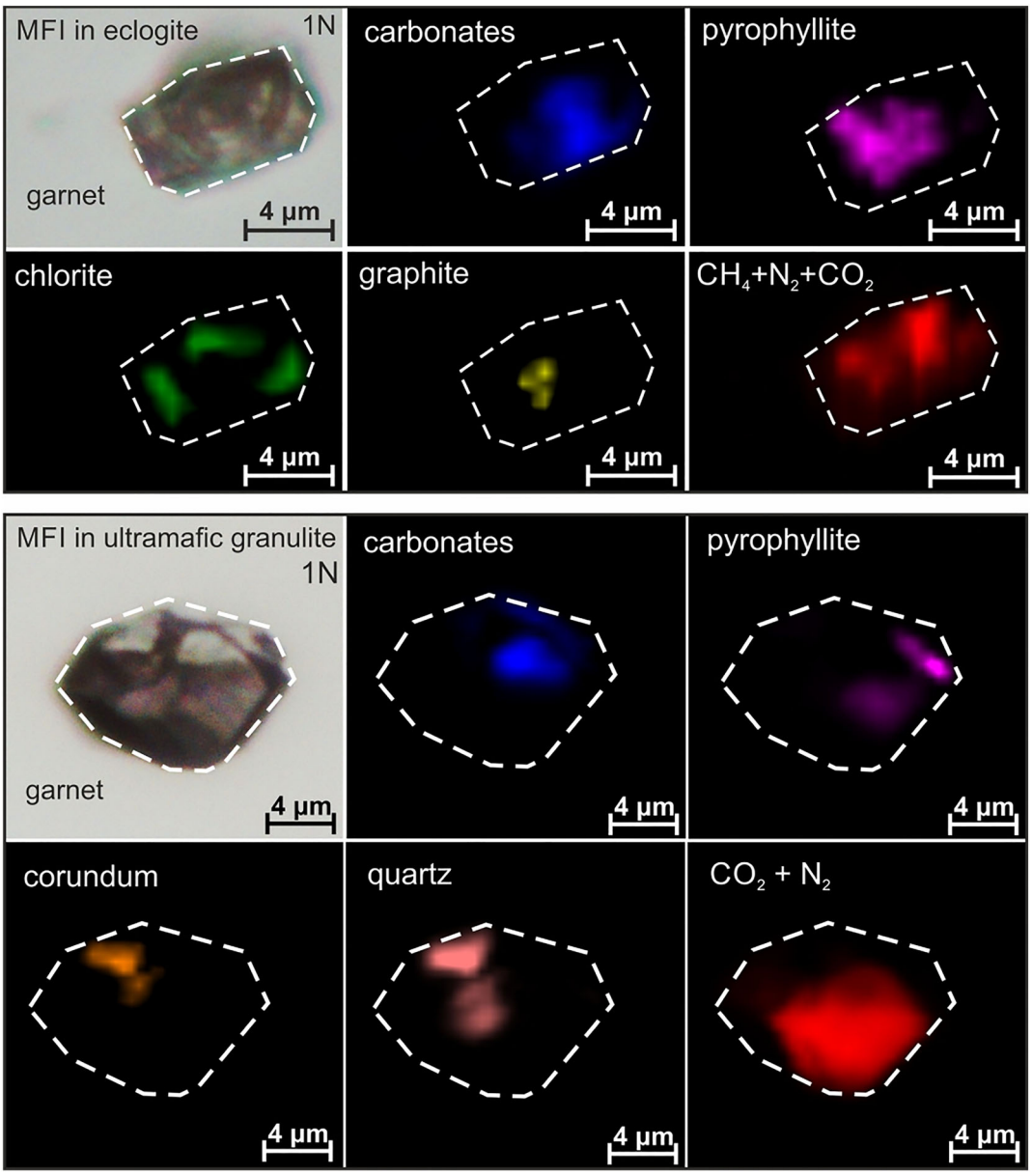

FIGURE 6 Photomicrograph (plane-polarized light) and Raman images showing the distribution of solid and fluid phases in a multiphase fluid inclusion (MFI) in garnet of the studied eclogite and ultramafic granulite, respectively. Intensity of the colors refers to the abundance of constituents of the inclusions [Colour figure can be viewed at wileyonlinelibrary.com]

ratios in MFI, that is, 56:44 for ankerite and siderite, respectively (in MFI in ultramafic granulite and 48:52 for ankerite and siderite, respectively). The morphology of pyrophyllite is fibrous and lamellar, whereas in eclogite, it forms an intergrowth with chlorite (Figure 7a–c). In intermediate granulite, pyrophyllite is interlayered with a Ca-bearing phyllosilicate (Figure 7f), confirming the occurrence of margarite in agreement with Raman spectroscopy (Figure 4). Characteristics SEM-EDS spectra of the dominant mineral phases are provided in Figure S3. On the basis of SEM imaging, MFI have numerous small cavities between solid phases and at the wall of the inclusion (Figure 7d), which corresponds to the location of the fluid phases (Figure 6). Approximately 10–50 nm sized spherical-hexagonal particles of graphite have been found in some of these cavities (Figure 7d). Furthermore, pyrite with traces of Cu and As has been observed at the walls of the inclusions with a size ranging between 100 and 300 nm. A few submicron-sized (100–200 nm) spots of apatite and rutile (accidentally trapped minerals) have also been detected.

Application of SEM image analyses with labeling of distinct phases on each equidistant slices allowed 3D reconstruction of the inclusions and determination of

TABLE 2 Estimated relative proportions of solid and fluid phases based on Raman imaging and FIB-SEM analyses on primary MFI in garnet of eclogite and granulites from COC

	Eclogite					Ultramafic granulite				Intermediate granulite			
	Raman area%			FIB vol.%		Raman area%			FIB vol.%	Raman area%			FIB vol.%
	($n = 30$)					($n = 9$)				($n = 6$)			
	min	max	aver	FIB1	FIB2	min	max	aver	FIB01	min	max	aver	FIB01
Carbonates	22	45	30	29	31	21	38	30	34	27	36	31	30
Pyrophyllite	18	31	24	30	34	7	18	12	6	20	31	27	33
Chlorite	0	19	8	18	17	-	-	-	-	-	-	-	-
Corundum	0	3	<1	-	-	0	13	6	8	-	-	-	
Quartz	-	-	-	-	-	0	27	13	21	-	-	-	-
Margarite	-	-	-	-	-	-	-	-	-	0	11	6	3
Graphite	0	13	4	<1	<1	0	8	1	-	0	2	<1	-
Pyrite	0	1	<1	<1	<1	0	1	<1	<1	0	1	<1	<1
Fluids ($N_2 \pm CO_2 \pm CH_4$)	21	46	32	23	18	15	40	38	31	23	38	34	34

Note: Results are derived from calculation using pixel count of the area size of each solid and fluid phase obtained with Raman images (area%) and FIB serial sectioning (FIB1–2 vol.%). Presented 2D Raman images have been carried out in one certain depth of the inclusion and accidentally trapped solid phases (except for quartz in ultramafic granulite) are not considered here.
Abbreviation: aver, average; COC, Cabo Ortegal Complex; max, maximum; min, minimum; n, number of analyses.

precise volumetric ratios in MFI (Figure 8, Table 2). Volume percentages in eclogite (COC17-062, Figure 8a,c) are as follows: 29%–31% carbonates, 30%–34% pyrophyllite, 17%–18% chlorite and 18%–23% cavity (fluid), whereas graphite, sulfide and accidentally trapped solid phases do not exceed 1%. In the ultramafic granulite sample (COC17-079a, Figure 8b,e), the following volume distribution has been acquired: 34% carbonates, 6% pyrophyllite, 8% corundum, 21% quartz and 31% cavity (fluid), whereas the volume of pyrite and other accidentally trapped minerals is <0.5%. MFI in the intermediate granulite sample (COC17–060b, Figure 8c) is composed of 30% carbonates, 33% pyrophyllite, 2.5% margarite and 34% cavity (fluid), whereas pyrite and accidentally trapped solid phases do not exceed 0.5%. Corundum was also confirmed with Raman spectroscopy in some MFI from eclogite, but it has not been identified during serial sectioning, except in the ultramafic granulite sample (Figure 7e).

5.5 | Approach used to estimate bulk MFI composition

We estimated the bulk compositions of individual MFI in terms of the major elements using the modal proportions of the solid and fluid phases in the MFI and their composition obtained by means of EDS-SEM. Modal proportions of the phases in the MFI were obtained by Raman 2D imaging ($n = 30$ and $n = 9$, for the eclogite and ultramafic granulite hosted MFI, respectively) under the assumption that relative areas can be extrapolated to volume proportions. This assumption is supported by the good agreement between area and volume proportions obtained by either Raman imaging or FIB sectioning (see Tables 2 and S3) on selected MFI. In detail, the procedure we applied was as follows: (1) computing the mass of an (arbitrary) 100 cm^3 of all investigated MFI (Table S4, column "Mass g/100 cm^3") using the normalized vol.% (taken from the area %) of the identified phases (Table S4) and the density of the solids at ambient conditions (taken from the Holland & Powell, 2011 database, Table S8) and the density of the residual fluid phase (Table S7) assumed to be at a pressure of 500 bar based on Raman shifts (Tables S10 and S11, see also more details in Appendix S2), (2) computing the volume per kg of MFI of individual phases and the fluid (Table S5) by normalizing the vol.% of the individual phases to one kg using the total mass for 100 cm^3 of MFI obtained in the previous step, (3) expressing the amount of individual phases in mol/kg of MFI (Table S6) using the molar volume for individual phases and endmembers of the gas at 500 bar (cm^3/mol, Table S8) and finally, (4) the mol/kg of the components Ca-Mg-Fe-Al-Si-H_2-O_2-C-N_2 for the MFI (Table S9) was found by using the atoms per formula unit of the mineral phases and the fluid molar composition

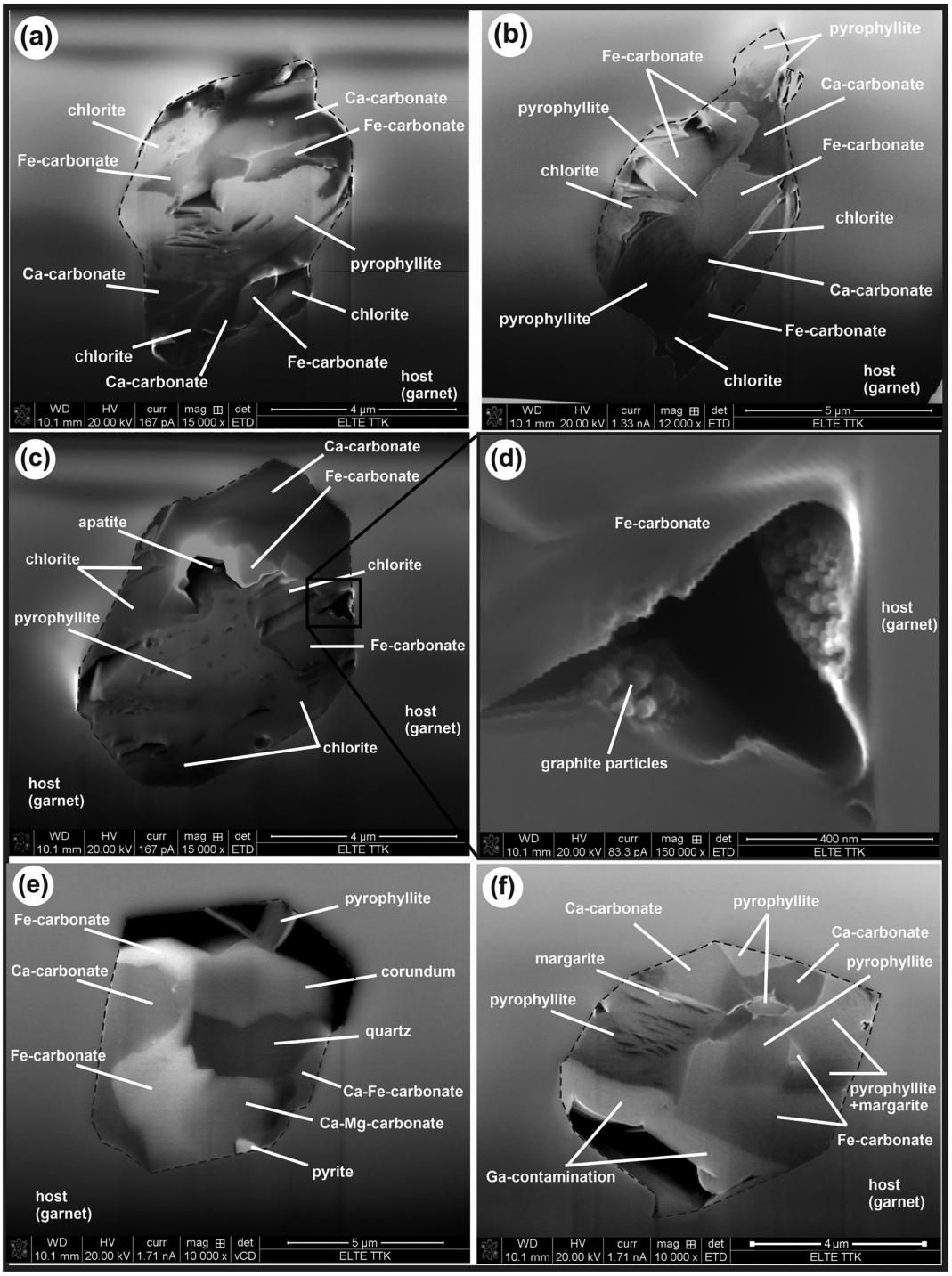

FIGURE 7 Representative images on slices of multiphase fluid inclusions (MFI) from each studied rock type (a–d, eclogite: COC17-062e, ultramafic granulite: COC17-079a and f, intermediate granulite: COC17-060b) taken during FIB-SEM analyses. (a–c) Secondary electron images showing tight intergrowth of Fe-Ca-Mg-carbonates, pyrophyllite and chlorite in MFI in eclogite; (d) close-up view of the black square on image (c) showing an exposed cavity with few tens of nanometer-sized graphite particles on the walls of the void, filled with fluid before exposure (SE image); (e) BSE image showing intergrowth of Fe-Ca-Mg-carbonates, pyrophyllite, corundum and quartz in MFI of ultramafic granulite; (f) a representative slice of MFI in intermediate granulite (BSE image) showing an intergrowth of carbonates and phyllosilicates (margarite is interlayered with pyrophyllite). Dark areas are voids exposed during serial sectioning, which contain a fluid phase ($N_2 \pm CH_4 \pm CO_2$), presented in Table 1 and Figures 4 and 5

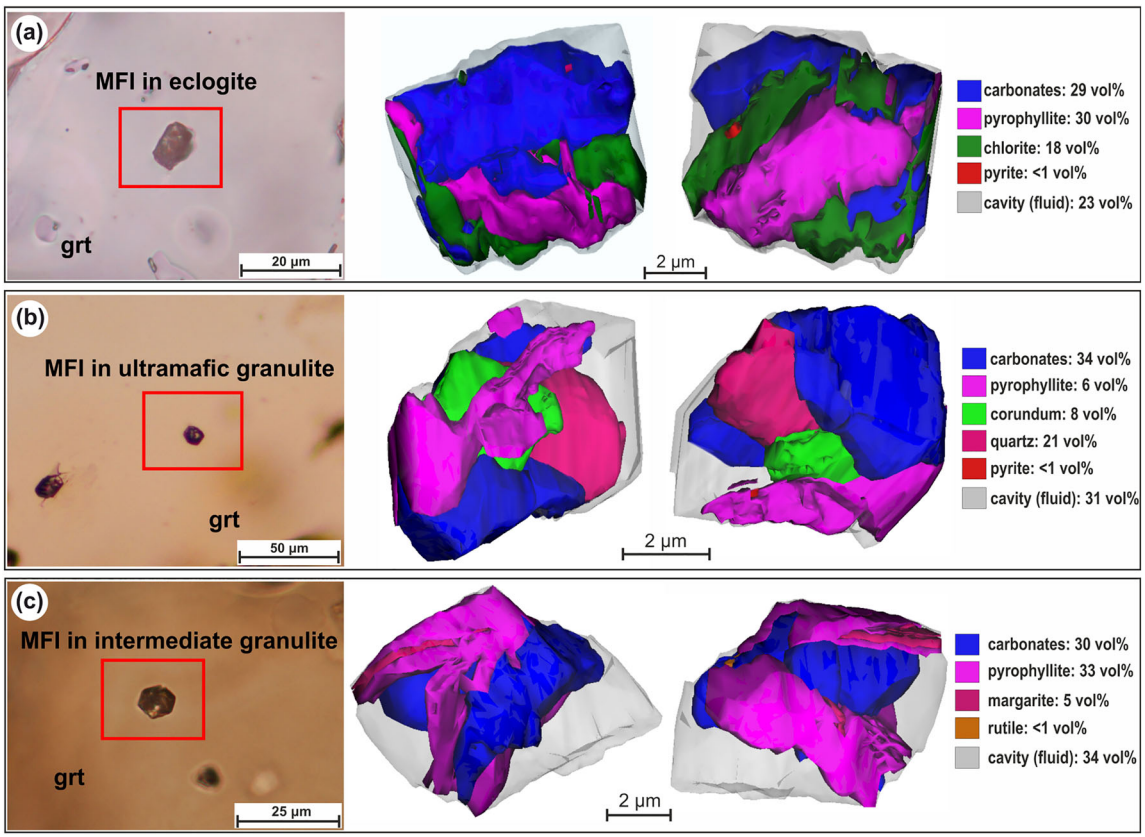

FIGURE 8 Photomicrographs and 3D reconstructions of representative multiphase fluid inclusions (MFI) in eclogite (a: COC17-062) and granulites (b: COC17-079a and c: COC17-060) in two different random views (characteristic for distribution of the coexisting solid and fluid phases). The inclusions were exposed with FIB-SEM serial sectioning and volume ratios of the phases, and 3D view was obtained using Reconstruct software [Colour figure can be viewed at wileyonlinelibrary.com]

(Table S8). Details about the choice of molar volume for solids and the residual fluid can be found in the supporting information (Appendix S2). The use of elements instead of conventional weight of oxides to define the bulk composition is preferred when using electrolytic thermodynamic modelling (Connolly & Galvez, 2018). The pseudosection presented in the main text (Figure 10) was computed assuming a simple molecular fluid model, but for comparison, we present the results of the electrolytic model using the lagged minimization algorithm for two representative HP-HT and LP-LT conditions (Table 3).

6 | DISCUSSION

6.1 | Origin of MFI and fluid composition

Room temperature phase assemblages of the studied MFI show similar features of multiphase solid inclusions (MSI) described in UHP rocks (e.g. Frezzotti & Ferrando, 2015; Philippot & Selverstone, 1991). MSI are thought to represent a homogeneous solute-rich supercritical aqueous fluid at entrapment (Ferrando et al., 2005; Frezzotti & Ferrando, 2007; Maffeis et al., 2021; Hermann et al., 2006; Zheng & Hermann, 2014). By contrast, MFI from this study comprise a ubiquitous and constant presence of fluids in the studied rock types (Tables 1 and 2). Additionally, MSI have been recorded only in UHP rocks (Frezzotti & Ferrando, 2015), whereas peak metamorphic conditions obtained in eclogites from the COC did not exceed 2.2 GPa (Mendia, 2000) and 1.7 GPa for granulites (Puelles et al., 2005), thus making less likely the direct precipitation from oversaturated aqueous fluid (daughter origin) as the only mechanism for producing the observed MFI. Multiphase inclusions were previously recorded in HT granulite facies rocks that experienced anatexis (Carvalho et al., 2019; Ferrero et al., 2014; Tacchetto et al., 2019). These MFI generally coexist with nanogranitoids (Acosta-Vigil et al., 2016; Carvalho et al., 2019, 2020; Cesare et al., 2007, 2015; Ferrero et al., 2014; Tacchetto et al., 2019), in which inclusions

TABLE 3 Modal proportions, mineral composition and phase speciation of stable phases modelled using electrolytic modelling of MFI_FIB1 bulk composition at both low and high P-T conditions, as indicated with green and yellow stars on Figure 10, respectively.

Phase composition (molar proportions):														
T = 800°C and P = 18 kbar (yellow star in Figure 10)							**T = 320°C and P = 5 kbar (green star in Figure 10)**							
	Dol	**Mgs**	**Grt**	**Cpx**	***F***	**Gr**	**Dol**	**Mgs**	***F*1**	***F*2**	**Chl**	**Prl**	**Qz**	**Gr**
wt.%	4.51	2.49	64.23	6.61	19.82	2.34	20.66	10.39	1.92	2.88	38.52	6.22	17.05	2.36
vol.%	4.02	2.01	42.89	5.22	43.23	2.63	17.96	7.47	5.30	8.44	34.87	5.94	17.27	2.77
mol%	2.08	2.35	12.45	2.65	63.02	17.44	10.58	9.82	10.53	11.02	6.45	1.79	29.44	20.38
Ca	1.0000	0.0000	0.3506	1.0000	*0.0984*	0.0000	1.0000	0.0000	*0.0152*	*0.0000*	0.0000	0.0000	0.0000	0.0000
Mg	0.6950	0.6621	0.9483	0.7080	*0.0679*	0.0000	0.4225	0.1911	*0.0023*	*0.0000*	2.0215	0.0000	0.0000	0.0000
Fe	0.3050	0.3379	1.7012	0.2181	*0.0034*	0.0000	0.5775	0.8089	*0.0329*	*0.0000*	1.9851	0.0000	0.0000	0.0000
Al	0.0000	0.0000	2.0000	0.1478	*0.0006*	0.0000	0.0000	0.0000	*0.0002*	*0.0000*	3.9870	2.0000	0.0000	0.0000
Si	0.0000	0.0000	3.0000	1.9261	*0.5388*	0.0000	0.0000	0.0000	*0.0704*	*0.0016*	2.0065	4.0000	1.0000	0.0000
H_2	0.0000	0.0000	0.0000	0.0000	*3.9951*	0.0000	0.0000	0.0000	*9.9756*	*2.2424*	4.0000	1.0000	0.0000	0.0000
O_2	3.0000	1.5000	6.0000	3.0000	*71.3636*	0.0000	3.0000	1.5000	*82.0979*	*33.0454*	9.0000	6.0000	1.0000	0.0000
C	2.0000	1.0000	0.0000	0.0000	*14.7343*	1.0000	2.0000	1.0000	*1.0829*	*5.7612*	0.0000	0.0000	0.0000	1.0000
N_2	0.0000	0.0000	0.0000	0.0000	***9.1981***	0.0000	0.0000	0.0000	*6.7227*	***58.9494***	0.0000	0.0000	0.0000	0.0000
Phase speciation (in mol %):														
	dol: 69.50	mgs: 66.21	alm: 56.70	di: 70.80	H_2O: 55.57		ank: 57.73	sid: 80.89	H_2O: 93.67	**N_2: 56.97**	ame: 99.45			
	ank: 30.50	sid: 33.79	py: 31.61	hd: 21.81	CO_2: 34.42		dol: 42.27	mgs: 19.11	N_2: 4.52	H_2O: 30.01	dph: 39.70			
			grs: 11.69	cats: 7.39	**N_2: 9.21**				CO_2: 1.66	CO_2: 12.96	afchl: 0.10			
					CO: 0.10				CH_4: 0.00	CH_4: 0.03	clc: −39.24			
					NH_3: 0.10									
					CH_4: 0.06									
					H_2: 0.03									

Note: Composition of the phases are in atoms per formula unit (apfu), except for the fluid phase (*F at HP-HT conditions and F1, F2 as two immiscible fluids at LP-LT conditions*), that is in wt.%. Variation of nitrogen content is highlighted with bold. Mineral abbreviations are after Whitney and Evans (2010), except for specific and fictive endmembers of solid solutions from Holland & Powell (2011) database and related works as used by Perple_X.

are defined as crystallized silicate melt, thus indicating fluid-melt immiscibility (Cesare et al., 2015; Korsakov & Hermann, 2006). In our study, however, no petrographic evidence of partial melting and no nanogranitoid inclusions were observed. Thus, it is unlikely that MFI characterized in this study are products of fluid-melt immiscibility.

Textural observations strongly suggest that MFI in garnet of eclogite and granulites from the COC have primary origin (Figure 3) and indicate entrapment during garnet growth likely at prograde-to-peak metamorphic stage (Frezzotti & Ferrando, 2015; Roedder, 1984). Similar but distinct solid phase assemblages of MFI (dominated by carbonates and phyllosilicates, Figure 4) and their nearly constant volume proportions (Table 2) indicate that a homogeneous fluid was trapped in the garnets. This is further supported by the fact that neither carbonates nor phyllosilicates have been found in the matrix rock as rock-forming minerals or crystal inclusions independently of MFI. Furthermore, solid phases in MFI have the same major to minor elements (Fe, Mg, Ca, Al and Mn) as that of the host garnet (Table S2). All of these suggest that minerals in the studied MFI are the result of a post-entrapment reaction of the trapped fluid with the host garnet (step-daughter minerals). The possibility of different post-entrapment modifications, local fluid–host mineral interactions and re-equilibration producing step-daughter crystals during exhumation processes has already been proposed for fluid inclusions in HP metamorphic rocks (Bodnar, 2003; Frezzotti & Ferrando, 2007; Maffeis et al., 2021; Philippot & Selverstone, 1991; Roedder, 1984; Scambelluri & Philippot, 2001; Touret, 1981, 2001).

Chemographic analysis of the MFI bulk chemical composition in eclogite and ultramafic granulite (Figure 9 and Table S9) shows that they are compatible with a garnet + COHN fluid composition (i.e. a mix between garnet and the line joining CO_2-H_2O on Figure 9b). Some of the bulk MFI compositions containing significant enrichment of graphite (5%–12% in modal proportions based on Raman imaging) fall out of the projected garnet-CO_2 tieline (Figure 9). Graphite content may be significantly overestimated during measurements with Raman spectroscopy, due to its fairly high Raman activity, in agreement with very low bulk graphite contents obtained by means of FIB analyses in MFI from eclogite. Modal proportion of graphite based on Raman imaging was estimated to be around 10 area % in two MFI from eclogite, whereas FIB analyses revealed that the real graphite content of the same inclusions is below <1 vol.% (Table 2). Overestimation of graphite can be explained by its high Relative Raman Cross Section, as a similar phenomenon of different gases and liquids (e.g. Haskin et al., 1997; Schrötter & Klöckner, 1979). Therefore, the graphite-enriched MFI compositions are considered biased by the Raman measurements and are not further considered.

The observed assemblage of the MFI in eclogite can be reproduced with comparable volume proportions at 0.5 GPa and 320°C (Figure 10) by thermodynamic modelling (molecular and electrolytic model) using the bulk composition determined by the FIB mineral proportions (MFI_FIB1 on Figure 9 and Table S9) as being a representative example for the MFI (Figure 10a,b and Table 3). Moreover, the modelled carbonate compositions in this low-pressure assemblage have similar compositions to the ones observed in the MFI based on EDS data ($ank_{58}dol_{42}$ vs. $ank_{50}dol_{50}$ and $sid_{80}mag_{20}$ vs. $sid_{70}mag_{30}$ for modelled and observed, respectively, Table 3). The model predicts a high amount of quartz, which is, however, in disagreement with most of the observations (Table 2). This discrepancy can be explained by the modelled chlorite composition, which is poorer in silica (2.0 Si apfu) relative to the measured composition (2.7–2.9 Si apfu; see Tables S2 and S8). The production of carbonates and hydrous silicates through the carbonation and hydration reaction of the almandine endmember in garnet with CO_2 and H_2O was previously proposed by thermodynamic calculations in simple systems (Carvalho et al., 2020; Marini, 2007). At peak conditions (1.8 GPa, 800°C), the modelled assemblage is largely (>85 vol.%) formed by garnet and a COHN-fluid (Figure 10b) supporting a homogeneous entrapment of a fluid composed mostly of H_2O (56 mol%) and CO_2 (34 mol%) with additional N_2 (10 mol%, Figure 10c, Table 3). The occurrence of other minor minerals, such as clinopyroxene (5.2 vol.%), carbonates (6.0 vol.%) and graphite (2.6 vol.%) suggests either (1) a slightly incorrect bulk composition estimate from the FIB-based MFI data or (2) that the original fluid was more enriched in H_2O (somewhere along the tieline joining the MFI and H_2O, Figure 9), which can be explained by a partial H_2O loss. Computations using either molecular fluid or electrolytic aqueous solutions do not significantly modify these volume proportions (compare Tables 3 and S12). Preservation of the original amount of H_2O in inclusions formed at high P–T conditions is quite rare, together with the general process of selective H_2O loss from fluid inclusions during exhumation (e.g. Frezzotti et al., 2012; Frezzotti & Ferrando, 2015; Hall & Sterner, 1993; Hidas et al., 2010; Maffeis et al., 2021). Various mechanisms of reequilibration (decrepitation, leakage by nanocracks/dislocations or diffusion) during post-entrapment evolution of fluid inclusions may simultaneously operate and cannot be observed under optical microscopy (Bakker & Jansen, 1994; Bodnar, 2003; Roedder, 1984; Viti &

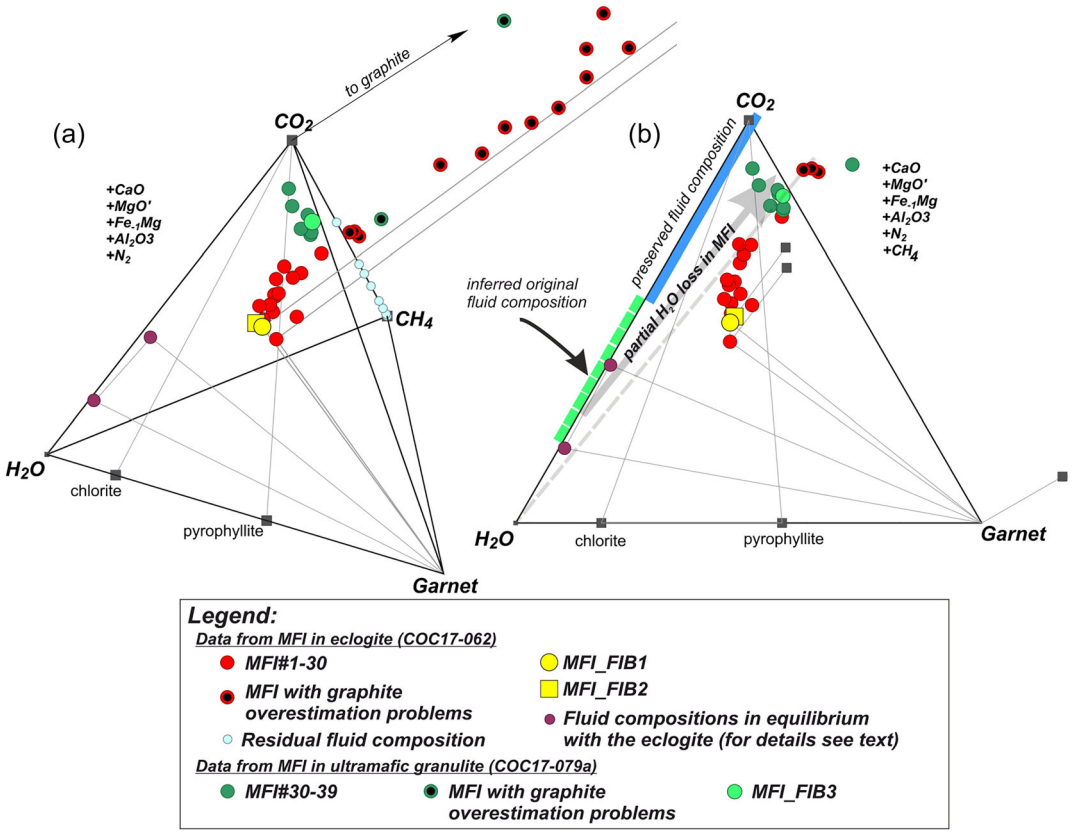

FIGURE 9 Compatibility diagrams (chemographies) constructed after reducing the compositional space to four (a) and three (b) components (projection phases and exchange vectors are indicated), showing individual estimates of the bulk multiphase fluid inclusions (MFI) compositions for eclogite and ultramafic granulite (see Legend) based on molar proportions in the CaFMAS-COHN system with the measured compositions of carbonate, chlorite and pyrophyllite by EDS (for dataset see Table S2). Most of the values for MFI in eclogite fall into the chlorite–pyrophyllite–siderite–magnesite (CO_2) triangle lying between the endmembers of garnet and H_2O-CO_2 fluid composition. All of those points falling out of the chlorite–pyrophyllite–siderite–magnesite (CO_2) triangle are MFI with high (5%–12% in modal proportions) and potentially overestimated graphite content (Table 2). The lines ending with black squares are tielines joining the garnet and MFI with the graphite that due to the projection from methane it plots at the infinity. Dashed grey line indicates a trend of potential H_2O loss, which is paralell with a line connecting bulk MFI data points with modelled fluid compositions in equilibrium with the eclogite. The purple circles correspond to these modelled fluid compositions using different CO_2 contents in equilibrium with the eclogite; for details, see text and Appendix S3 and Figure S1. Compatibility diagrams were plotted using CSpace (Torres-Roldán & Garcia-Sanchez, 2000) [Colour figure can be viewed at wileyonlinelibrary.com]

Frezzotti, 2001; Yamamoto et al., 2011). Different degrees of leakage and decrepitation further depend on the size of the inclusions, that is, smaller inclusions are more prone to 'survive' without decrepitation (e.g. Campione et al., 2015). Loss of H_2O may take place not only by optically visible or nanoscale decrepitation of inclusions but also by other processes such as passive diffusion to the host mineral due to the small size of hydrogen protons (Bodnar, 2003; Mavrogenes & Bodnar, 1994).

In addition to MFI in eclogite, thermodynamic modelling, using bulk composition of a representative multiphase fluid inclusion in ultramafic granulite, presented in Figure S4 (MFI_FIB3 on Figure 9) confirms that post-entrapment reactions are likely to have evolved in a similar way to that observed for the MFI in the eclogite. The assemblage pyrophyllite + two carbonates (dolomite-ankerite and magnesite-siderite solid solutions) +- quartz + kyanite + minor hematite (and residual N_2-enriched fluid) can be reproduced at low P–T conditions similar to the one inferred for MFI in eclogite (Figure 10a). The absence of chlorite in the modelled assemblage also agrees with the observations. However, corundum instead of kyanite occurs in all studied MFI. The production of kyanite instead of corundum + quartz in the MFI may be controlled by the metastable behaviour of the aluminosilicate polymorphs due to the extremely small size of inclusions as discussed by Carvalho et al. (2020). At peak conditions, the modelled assemblage has dominantly a garnet and COHN-fluid composition (52.97 + 38.19 vol.%, respectively), together

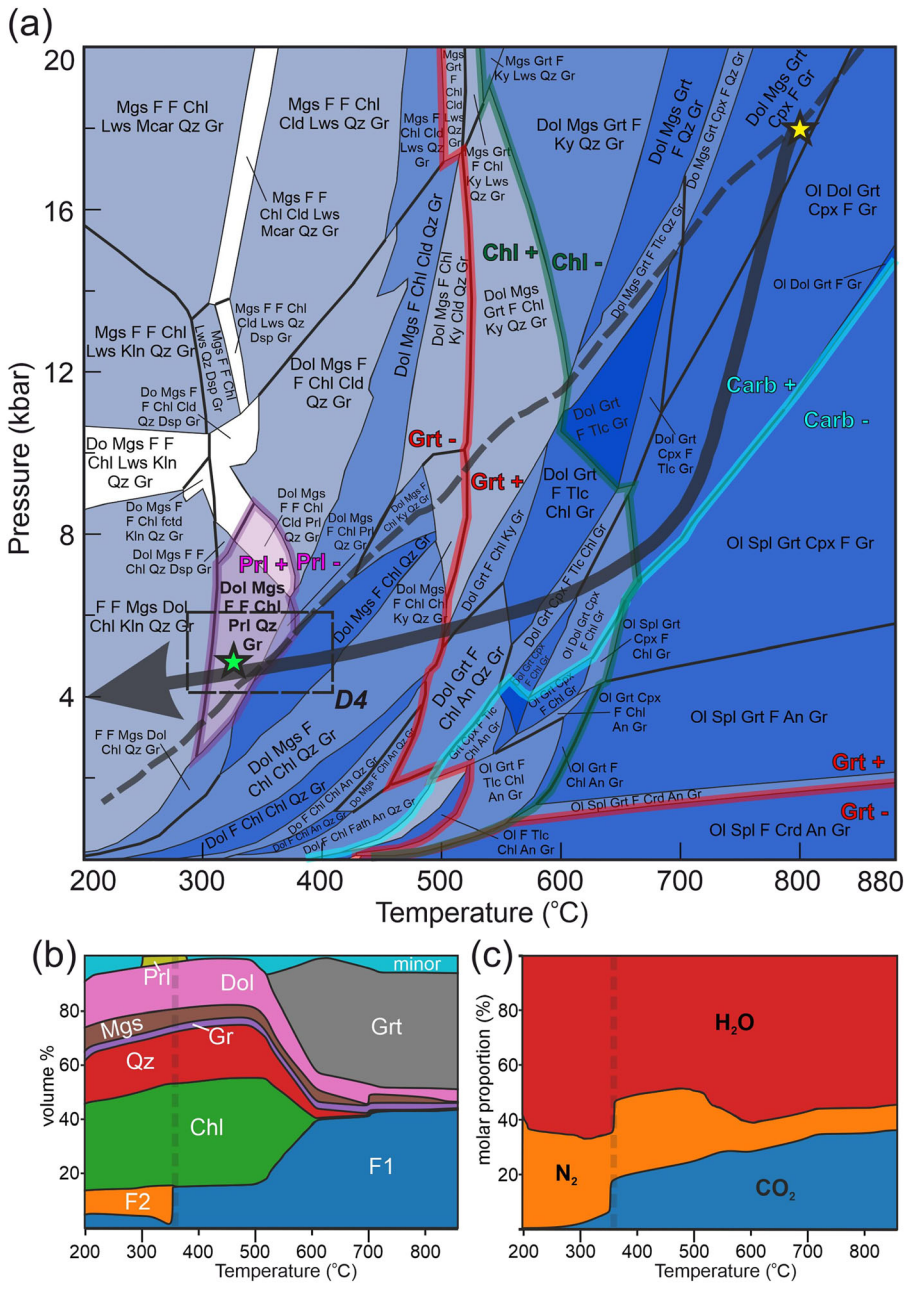

FIGURE 10 (a) Pseudosection of a representative multiphase fluid inclusions (MFI) bulk composition in eclogite (MFI_FIB1 on Figure 9a,b). The stability fields of carbonates, chlorite, pyrophyllite and garnet are indicated (with colored lines). Color blue levels indicate the variance of the assemblage (the darker the higher the variance). Carb designates the presence/abscence of any of the two carbonates. Dashed grey line represents an iso-density path for the whole system (2,637 kg/m^3) along which the proportions of the solid and fluid phases are presented in Figure 10b,c. Retrograde PT-path of the rock and dashed rectangle indicate the range of D4 deformation phase recorded in the COC, after Puelles et al. (2005). (b) Distribution of volume proportions of the solid phases along the iso-density path for the whole system (2,637 kg/m^3 Figure 10a) of MFI_FIB1 bulk composition in eclogite. Minor phases are consisted of kyanite, talc and chloritoide. Dashed grey lines on (b) and (c) indicate the beginning of fluid immiscibility along the retrograde path, which may correspond with the stability zone of pyrophyllite. Modal proportions, mineral composition and phase speciation of stable phases at two representatives high-pressure–high-temperature (HP-HT) and low-pressure–low-temperature (LP-LT) conditions are presented in Tables 3 and S13. (c) Distribution of molar proportions of the fluid phases along the iso-density path for the whole system (2,637 kg/m^3 Figure 10a) of MFI_FIB1 bulk composition in eclogite. The fluid is in molar basis and is the average of the two immiscible fluids for the last part of the decompression path. Even though the enrichment of N_2 and consumption of CO_2 with decreasing temperature fits well with our observations in the MFI, the modelled H_2O and CH_4 contents for low temperatures show a disagreement; furthermore, the change of CH_4 content could not be represented as having insignificantly low amounts in the model. This could be explained by the H_2O loss, as well as our little constrain on oxygen fugacity during the retrograde path (for details see text) [Colour figure can be viewed at wileyonlinelibrary.com]

with other minor phases such as dolomite (4.72 vol.%), kyanite (1.66 vol.%) and quartz (2.46 vol.%), which indicate a similar homogeneous entrapment together with an even higher degree of partial loss of H_2O.

The formation and development of secondary MFI in pyroxenites may be possibly explained by similar post-entrapment processes affecting an originally trapped H_2O and CO_2-bearing fluid. The host mineral, nearly pure diopside (Tilhac et al., 2016, 2017), could have allowed step-daughter phases to take-up elements like Ca and Mg, thus production of calcite ($CaCO_3$) and talc ($Mg_3Si_4O_{10}[OH]_2$) via carbonation and hydration reactions, possibly as analogous mechanism evidenced in orthopyroxene described by Frezzotti et al. (2012).

To have an independent constraint on the potential original composition of the trapped fluid, we made a comparison to assess if the obtained fluid composition in eclogite (H_2O: 56 mol%, CO_2: 34 mol% and N_2: 10 mol%) at HP from the MFI bulk composition hosted in garnet could be compatible with a fluid in equilibrium with the bulk eclogite assemblage (Appendix S3 and Figure S1). This was calculated based on bulk rock data of Gil Ibarguchi et al. (1990) and implies that a value higher than 25 mol% CO_2 content in the fluid is compatible with the eclogite mineral assemblage devoid of zoisite (plotted on Figure 9) at peak conditions (i.e. 800°C and 18 kbar; see Appendix S3, Figure S1 and Table S14–15 for futher details). The results of thermodynamic modelling on the composition of the trapped fluid at HP-HT conditions (Figure 10c and Table 3) suggest a CO_2 content of 34 mol %, indicating a CO_2-bearing aqueous character. This fluid is characterized by a certain solute charge (2.8 mol/kg, Table S15) and could have been indeed in equilibrium with the bulk eclogite. Thus, there is no requirement for influx of an external fluid, or alternatively, the external fluid, if any, should have equilibrated with the bulk eclogite before the entrapment.

6.2 | Formation of solids within the MFI

As stated above, carbonates and sheet silicates within the MFI (Figures 3, 4, 6 and 7) are clearly step-daughter minerals. Nevertheless, minerals (i.e. quartz, rutile and apatite) that are both present in MFI and in the host garnet as crystal inclusions (Figure 3b) can be considered partially as accidently entrapped minerals in each rock type. However, the presence of quartz with corundum (Figure 7e) was confirmed in the majority of MFI in ultramafic granulite. This indicates that in this rock, quartz can also be interpreted as a step-daughter mineral, similarly as described by Carvalho et al. (2020) and Tacchetto et al. (2019). According to the prediction of our model (Figure 10b and Table 3), such origin of quartz is possible in the MFI in eclogite too, without considering accidental entrapment. Furthermore, solid phases in the MFI could have also precipitated from the COHN fluid in minor fractions. Enhanced solubility of elements, like Si, Al or Fe, in our case, in H_2O at HT-HP conditions has been proposed by several authors (e.g. Dolejš & Manning, 2010; Kessel et al., 2004; Manning, 1994; Newton & Manning, 2003) accounting for the possible crystallization of daughter minerals directly from the trapped fluid. It may be especially true for quartz due to high solubility of Si in H_2O at these conditions. This is also supported by the non-trivial charge of solute computed for the eclogitic assemblage at peak conditions (approximately 2.8 mol/kg, Table S15). Interestingly, the modelled solute charge of the new system (after entrapment) C-bearing fluid–garnet is significantly lower (approximately 0.184 mol/kg at peak conditions and nearly 0 at 320°C and 5 kbar, Table S13). It is highly likely that the trapped fluid, equilibrated with the eclogite, would additionally attain equilibrium with the host garnet. This process should result in precipitation of some of the observed solid phases, like quartz within MFI, as being one of the most abundant aqueous species in the trapped fluid (Table S15). However, it can only represent a minor fraction of the observed MFI assemblage as the peak conditions of the COC eclogite (18 kbar and 800°C, Gil Ibarguchi et al., 1990) suggest maximum solubilities of approximately 6 wt.% of Si in the aqueous fluid (Tables S14 and S15), whereas an overall 20 wt.% of C-bearing fluid supposedly reacts with 65 wt.% of garnet (Table 3). Our calculations nevertheless clearly indicate that bulk chemical composition of the studied MFI (Figure 9 and Table S9) is consistent with a garnet + COHN fluid composition. This implies that step-daughter producing post-entrapment reactions can be considered as plausible dominant processes, which are responsible for the formation of the MFI, without excluding the possibility of minor production of daughter minerals.

6.3 | Timing of MFI crystallization

According to the observed intricate intergrowth of the solid phases (Figure 7), it is highly likely that the mineral assemblage in the MFI precipitated together in a single step as there is not any sign of systematic zonation or a traceable sequence of solid phases inside the MFI (Figure 7a,c), which would be a result of sequential crystallization or periodic precipitation as evidenced in MSI in pyrope from Dora Maira whiteschist (Frezzotti & Ferrando, 2015). Under equilibrium conditions, carbonates and chlorite would be expected to crystallize earlier

at temperatures higher than pyrophyllite (> 600°C, Figure 10) in MFI in the eclogite. This seems unlikely as (1) microstructure of the inclusions does not support this interpretation (see above and Figure 7) and (2) there is no trace of other solid phases in the observed assemblage, such as kyanite, talc or chloritoide which all would appear at higher temperatures if equilibrium would have been attained continuously during decompression (Figure 10). Thus, it is inferred that carbonates and chlorite have possibly remained at metastable state until reaching the stability field of pyrophyllite. Graphite is predicted to be stable in a low-pressure assemblage together with carbonates, pyrophyllite, chlorite and quartz; even the MFI bulk composition used for modelling was computed from a graphite-free assemblage. This type of metastable behaviour with delayed nucleation and crystallization may be possibly due to the small volume of the inclusions as suggested by Carvalho et al. (2020), together with other effects modifying the energy of the system, such as surface tension rather than the bulk Gibbs free energy. It cannot be ruled out that the metastable crystallization could be linked to or even triggered by the H_2O loss from the MFI and/or a deformation episode during exhumation. This latter possibility may correspond with a deformation phase, termed as D4 phase with extensional shear by Ábalos et al. (1996) and Puelles et al. (2005) during late retrogression of the HP units of the COC (Figure 10a). A fast reequilibration from a metastable state concomitant with the partial loss of H_2O could further explain the occurrence of CO_2 in the residual fluid that should have been consumed during carbonation at higher temperature (min. 500–700°C) than the maximum temperature stability of pyrophyllite (around 400°C) (Figure 10).

A further notable prediction of the thermodynamic model is that at temperatures below 350–400°C—corresponding to the stability field of pyrophyllite (Figure 10)—the residual fluid separates into two immiscible fluids: one fluid (F1) is nearly H_2O pure (approximately 94 mol%) and the other (F2) is a CO_2-bearing and is highly enriched in N_2 (up to 60 mol%) (Figure 10c and Table 3). This temperature range corresponds with the extended immiscibility field of the H_2O-CO_2 system for a wide P–TX range (Diamond, 2001; Hurai, 2010). An immiscible H_2O-rich fluid phase in the inclusion would further enhance both H_2O-loss from the MFI and sheet silicate producing reactions due to the increased activity of water. Wetting properties of H_2O account for distribution along the wall of the inclusion, easing its escape as a single phase through nanocracks/decrepitation. Equilibrium decompression path should produce a fluid, which is progressively enriched in H_2O (Figure 10c) contrary to the observations. When entering the stability field of pyrophyllite, there is an abrupt change in the composition of the fluid with CO_2 decrease, together with an increase of N_2. Nitrogen content is passively increased in the fluid due to the crystallization of carbonates and phyllosilicates. Enrichment of CH_4 (up to 87 mol% in the residual fluid phase) was also observed in MFI from eclogite (Table 1); nevertheless, its production is highly sensitive to certain redox conditions in the inclusions and precipitation of graphite (see below).

The lack of detectable H_2O as a fluid phase in the MFI, both in the eclogite and the granulites, could indicate that the fluid–garnet interaction ceased when H_2O was consumed in the reaction and hydration reaction produced pyrophyllite. Thermodynamic modelling (Figure 10c), however, suggests that CO_2 is almost fully consumed during the retrograde carbonation reactions; meanwhile, N_2-H_2O-enriched residual fluid is in equilibrium with the retrograde assemblage and is compatible with H_2O-saturated conditions. Similarly, enrichment of nitrogen in the fluid phase is also observed in the secondary inclusions in the studied pyroxenites of the COC (Figure 3e).

6.4 | Fluid regime at HP subduction zone conditions

Fluid inclusions witnessing N_2-rich retrograde and near peak fluids have been described in the Caledonides of Western Norway (Andersen et al., 1990, 1991; Jamtveit et al., 1990). Isochoric calculations of Andersen et al. (1991) indicate that the earliest high-density N_2-rich $\pm$ CO_2 fluid inclusions, trapped secondarily in quartz from eclogitic veins, represent early retrograde metamorphic fluids, possibly rather close to peak conditions (around 1 GPa and 600°C). Late-stage secondary fluid inclusions are rich in N_2, which are probably the result of decrepitation and redistribution of early fluid inclusions (Andersen et al., 1991). Although the presence of nitrogen-bearing fluids is a general feature of HP metamorphism (Andersen et al., 1989, 1990, 1991; Tomilenko & Chupin, 1983; Touret & Frezzotti, 2003), possible processes of abiotic N_2 enrichment in the fluid are not well constrained.

Fluid–rock interaction, similar to the reactions observed in the MFI, is highly likely to have affected the untrapped fluids as well in the subduction zone during their retrograde path. Similar partial or complete consumption of H_2O and CO_2 during retrograde evolution would designate a horizon (between 300°C and 400°C, below 1.0 GPa, Figure 11) of a fluid regime dominated or at least elevated in nitrogen, even though the nitrogen in

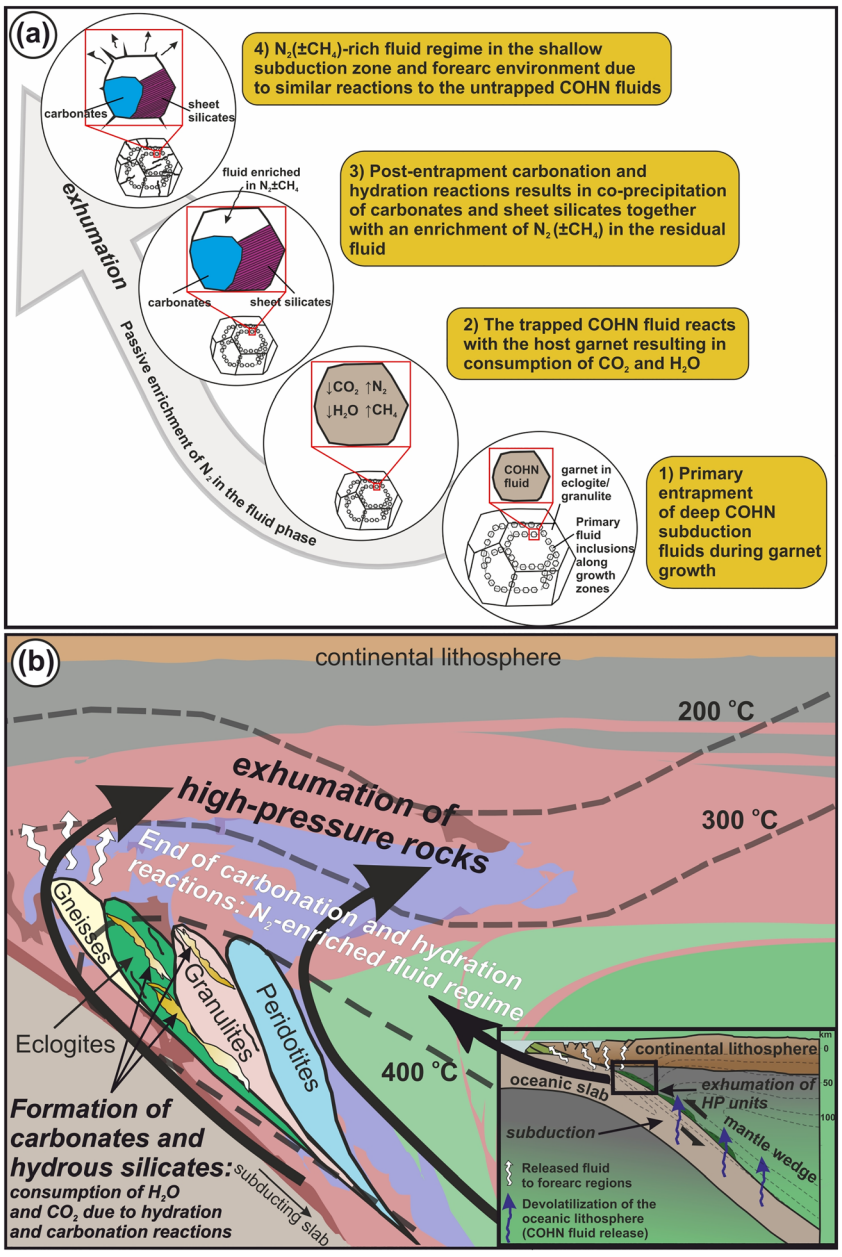

FIGURE 11 Schematic figure showing the proposed abiotic passive enrichment of $N_2 \pm CH_4$ in subduction zones. (a) Representative evolution model of $N_2 \pm CH_4$ enrichment during post-entrapment reactions observed in primary multiphase fluid inclusions (MFI) in high-pressure (HP) rocks from the Cabo Ortegal Complex (COC). (b) A simplified sketch showing the possible N_2 enrichment path, as a result of hydration and carbonation reactions, during exhumation of HP rocks (along the curved arrow) in the shallow subduction zone. Representation of isotherms in a subduction zone is based on Zheng (2019); contours of the mantle wedge (green for the lithospheric mantle and red-purple for HP tectonic mélange) during exhumation are drawn after Gerya (2019) [Colour figure can be viewed at wileyonlinelibrary.com]

the originally trapped fluid was probably present in minor amount.

The above-described fluid–rock interaction results in abiotic enrichment of not only nitrogen in the fluid phase but also methane especially in MFI in eclogite (comprising the residual fluid in 21–87 mol%). Such enrichment is not reproduced by our thermodynamic modelling where methane concentrations remain very low (Figure 10c and Table 3). The disagreement could be explained by our little constrain on oxygen fugacity during the retrograde path and for the neglected role of sulphur on redox conditions (Maffeis et al., 2021). Equally, the observed difference on the residual fluid composition between MFI of eclogite and granulite samples (Table 1) could be possibly explained by a difference of the initial composition of the fluid, that is, having various original ratio of H_2O-CO_2(-CH_4-N_2) and potentially different oxygen fugacity conditions in the different lithologies. Residual fluid composition of MFI in eclogite shows a slightly wider compositional range in CO_2-CH_4-N_2 content (Figure 5), which could be possibly due to small variations of N_2 in the trapped fluid and/or partial loss of H_2O after entrapment, resulting in a change in COH content and speciation in the fluid phase. Diffusion of elements (i.e. H) from the inclusions may result in a significant modification of the fluid composition and change the oxygen fugacity of the inclusion (Frezzotti & Ferrando, 2015). However, oxygen fugacity and activity of carbon during trapping of the COH fluid along with post-trapping re-equilibration and modifications may be potentially a

dominant factor for causing variations on the ratio of residual CO_2 and CH_4 in the inclusions (Hall & Bodnar, 1990). Methane, despite being quite uncommon, together with N_2 and CO_2 has been also identified as a significant constituent of prograde and peak metamorphic fluids in eclogite and granulite facies rocks (Carvalho et al., 2019; Fu et al., 2003; Maffeis et al., 2021; Mukherjee & Sachan, 2009; Tao et al., 2018). Abiogenic production of methane corresponds to reduction of carbonates (as the most abundant carbon-bearing phase in subduction environment) in the slab at HP-HT conditions with water saturation (Tao et al., 2018). Furthermore, the speciation of a carbon saturated COH fluid is controlled by the certain redox conditions of the system (Connolly, 1995; Galvez et al., 2013, 2016; Hall & Bodnar, 1990).

The presence of graphite in some of the MFI indicates that the trapped COH fluid became graphite saturated locally leading to its precipitation from the residual fluid during cooling and exhumation (Carvalho et al., 2019; Cesare, 1995; Cesare et al., 2007). As graphite coexists with methane-bearing residual fluid which is always connected to the small cavities between solid phases of the inclusions (Figure 7d), we assume that the fluid reached a saturation after the carbonation and hydration reactions and locally became graphite saturated in some of these cavities. This could have resulted in precipitation of graphite in some of the parts filled with residual fluid, explaining also small variations of fluid composition measured in a single multiphase fluid inclusion.

6.5 | Implications for nitrogen cycling

The behaviour of nitrogen during surface–subsurface biochemical reactions is relatively well understood; however, the knowledge about its global planetary cycle and the role of subduction as well as storage need further constraints (Bebout et al., 2013; Cannaò et al., 2020; Cartigny & Marty, 2013). Most studies agree that nitrogen input into the deep Earth is greater than outgassing (Busigny et al., 2011; Mitchell et al., 2010; Mysen, 2019; Sano et al., 2001), although Fischer et al. (2002) suggested a comparable extent of nitrogen subducted in sediments (i.e. clay minerals) versus nitrogen degassed by arc volcanism at the Central America convergent margin. As previously discussed, nitrogen is a commonly encountered constituent of fluids in subducted eclogite facies rocks. In the geological cycle of nitrogen, the initial source introduced into the subduction zone is organic material deposited in seafloor sediments (Bebout et al., 2013). During diagenesis and low-grade metamorphic evolution, nitrogen is released into pore fluids as ammonia (NH_3) then transforms into the form of ammonium (NH_4^+) (Busigny & Bebout, 2013; Cedeño et al., 2019). Having similar charge and ionic radius, the released NH_4^+ ion acts as an ideal substitution for K^+ in such phyllosilicates as clay minerals and micas, and alkali feldspars, confirmed by strong correlation between concentration of nitrogen and LIL elements, such as K, Rb and Cs (Busigny et al., 2003; Halama et al., 2010). The breakdown of micas during prograde metamorphism results in a continuous release of NH_4^+, although high stability of NH_4^+ under HP in white micas (phengite) or K-feldspar (hollandite) allows its retention to great depths (even of the transition zone) depending on redox conditions (Bebout, 2007; Cedeño et al., 2019; Watenphul et al., 2009). Efficiency of nitrogen release, which would equilibrate as N_2 (Li & Keppler, 2014), is mostly controlled by the breakdown of phengite, which is showing a strong correlation with the thermal gradient of subduction zones (Mitchell et al., 2010). Consequently, hot subduction paths promote a high degree of N escape, whereas cold geotherms enable the retention of NH_4^+ in HP micas or clay minerals resulting in efficient transport of nitrogen into great depths (Cedeño et al., 2019). Previous studies of Ábalos et al. (2003) and Puelles et al. (2005) highlighted that the studied suites of HP subducted rocks of the COC have been involved in prograde metamorphic evolution following a warm subduction PT path with 13–14°C/km, which would be sufficient for elevated N_2 release (Busigny & Bebout, 2013). Bulk N_2 concentration and stable nitrogen isotopic composition of eclogites from the COC described by Halama et al. (2010) reflect no further metasomatic addition (K-Rb-Cs-Ba) during subduction; overlap of N_2 concentration and $\delta^{15}N$ with data for the altered oceanic crust suites implies retention of seafloor-inherited N_2 to depth of around 90 km. Halama et al. (2010) further suggested that N_2 concentrations of 3–8 ppm hosted by fluid inclusions are required in COC eclogite because of the lack of phengite in these rocks. The present study confirms such inference (Figures 3b and 4). Accordingly, N_2 released from the slab would not fully return to the surface via arc volcanism, but HP subducted rocks can be a potential reservoir for N_2-rich fluids at shallower environment of the exhumation (Figure 11).

Our findings indicate a front at the temperature of 300–400°C, which is characterized by the enrichment of nitrogen during the exhumation path of HP rocks. The release of N_2-dominated fluids during retrograde processes may occur at shallower depths, resulting in enrichment of abiotic nitrogen in the fluid phase. This mechanism would serve to explain the presence of N_2-

rich fluids associated with HP serpentinization and would contribute to the elevated concentrations of nitrogen documented in serpentinized peridotites in subduction settings (Halama et al., 2012; Philippot et al., 2007; Vitale Brovarone et al., 2020). Prevalence of N_2 compared with H_2O and CO_2 in the fluid phase is witnessed in secondary fluid inclusions of pyroxenites as well, in accordance with retrograde metamorphic fluid compositions in the Caledonides (Andersen et al., 1991). Released or remobilized N_2-rich fluids may be channelized, transported and upflow providing contribution to the fluid regime of shallow subduction depths and even the subsurface environment (Figure 11). This conclusion is in good agreement with N_2-rich fluid composition of gas outflow of mud volcanoes and thermal springs at forearc regions of accretionary subduction complexes (Giggenbach et al., 1993; Lee et al., 2017; Motyka et al., 1989; Snyder et al., 2003), with reaching even 92 vol.% reported, for example, at the Andaman and Nicobar Islands (Chaudhuri et al., 2012). All of these suggest that such significant addition of nitrogen with deep subduction origin should play an important role in global nitrogen cycling and may provide significant contribution to N_2 supply to the overlying subsurface/surface biosphere during devolatilization in the forearc regions of convergent margins.

7 | CONCLUSIONS

The investigated primary MFI in eclogite and granulites and secondary MFI in pyroxenites from the COC represent trapped COHN fluids during prograde-to-peak metamorphism that were significantly modified by reactions with the host garnet during exhumation. Our results record a detailed characterization of microstructural, microchemical features, origin and post-entrapment evolution of primary MFI, together with thermodynamic modelling. The main implications of our study are summarized as follows:

- Trapped fluids can be described in the COHN system, where the dominant fluid components in the original fluid were H_2O and CO_2, whereas N_2 was present in minor amounts (H_2O: 56 mol%, CO_2: 34 mol% and N_2: 10 mol% in the studied eclogite). Thermodynamic modelling suggests that the trapped fluid should have been even more enriched in H_2O, compared with what is calculated for their bulk composition, implying a H_2O loss after entrapment by diffusion and/or cracks.
- During their post-entrapment evolution, this fluid has interacted with the host garnet during the exhumation path, resulting in (1) the formation of carbonates and phyllosilicates, (2) the passive enrichment of nitrogen in the residual fluid observed in the studied MFI (N_2 content: 13–68 mol% in the observed MFI) and (3) local enrichment of methane in MFI in eclogite (varying from 21 to 87 mol%).
- Thermodynamic models revealed that step-daughter assemblage is stable at low-pressure and low-temperature (between 2 and 9 kbar and 300–400°C) conditions. Our model and the microstructural data of the MFI suggest that the formation of the step-daughter minerals is expected at the same time due to metastable behaviour at higher pressure and temperature.
- A specific horizon in shallow subduction zone around 300–400°C (when crossing the stability field of pyrophyllite during exhumation path) can be marked as a nitrogen-enriched fluid regime. The release of these fluids may contribute to the understanding of N_2-rich fluid composition during devolatilization in the forearc regions of convergent margins.

ACKNOWLEDGEMENTS

The authors thank the reviewers Dr. Bruna Borges Carvalho, Dr. Simona Ferrando, Dr. Andrea Maffeis and the editor, Prof. Bernardo Cesare, for many valuable, constructive comments and suggestions which helped to improve the quality of the manuscript. The authors are thankful for the great help of Prof. Sándor Józsa during field work and sampling, as well as for support of the Lithosphere Fluid Research Lab. Márta Berkesi and Tamás Spránitz were partially supported by NKFIH_FK research funding number 132418. JAPN acknowledges financial support from the Spanish MICINN through the Ramón y Cajal fellowship (RYC2018-024363-I) funded by MICIN/AEI/10.13039/501100011033 and the FSE program ('FSE invierte en tu futuro'). This is the 107th publication of the Lithosphere Fluid Research Lab.

ORCID

Tamás Spránitz https://orcid.org/0000-0002-5086-3133
José Alberto Padrón-Navarta https://orcid.org/0000-0003-1005-0012
Csaba Szabó https://orcid.org/0000-0002-1580-6344
Ábel Szabó https://orcid.org/0000-0003-3031-4310
Márta Berkesi https://orcid.org/0000-0003-4380-057X

REFERENCES

Ábalos, B. (1997). Omphacite fabric variation in the Cabo Ortegal eclogite (NW Spain): Relationships with strain symmetry during high-pressure deformation. *Journal of Structural Geology*, *19*(5), 621–637. https://doi.org/10.1016/S0191-8141(97)00001-1

Ábalos, B., Azcarrage, J., Gil Ibarguchi, J. I., Mendia, M. S., & Santos Zalduegui, J. S. (1996). Flow stress, strain rate and effective viscosity evaluation in a high-presssure metamorphic nappe (Cabo Ortegal, Spain). *Journal of Metamorphic Geology*, *14*(2), 227–248. https://doi.org/10.1046/j.1525-1314.1996.59012.x

Ábalos, B., Fountain, D. M., Ibarguchi, J. G., & Puelles, P. (2010). Eclogite as a seismic marker in subduction channels: Seismic velocities, anisotropy, and petrofabric of Cabo Ortegal eclogite tectonites (Spain). *GSA Bulletin*, *123*(3–4), 439–456.

Ábalos, B., Puelles, P., & Gil Ibarguchi, J. I. (2003). Structural assemblage of high-pressure mantle and crustal rocks in a subduction channel (Cabo Ortegal, NW Spain). *Tectonics*, *22*(2), 1–21. https://doi.org/10.1029/2002TC001405

Acosta-Vigil, A., Barich, A., Bartoli, O., Garrido, C. J., Cesare, B., Remusat, L., Poli, S., & Raepsaet, C. (2016). The composition of nanogranitoids in migmatites overlying the ronda peridotites (Betic Cordillera, S Spain): The anatectic history of a polymetamorphic basement. *Contributions to Mineralogy and Petrology*, *171*(3), 1–31. https://doi.org/10.1007/s00410-016-1230-3

Albert, R., Arenas, R., Gerdes, A., Martínez, S. S., Fernández-Suárez, J., & Fuenlabrada, J. M. (2015). Provenance of the variscan upper allochthon (Cabo Ortegal Complex, NW Iberian Massif). *Gondwana Research*, *28*(4), 1434–1448. https://doi.org/10.1016/j.gr.2014.10.016

Andersen, T., Austrheim, H., Burke, E. A., & Elvevold, S. (1993). N_2 and CO_2 in deep crustal fluids: evidence from the Caledonides of Norway. *Chemical Geology*, *108*(1–4), 113–132. https://doi.org/10.1016/0009-2541(93)90320-I

Andersen, T., Austrheim, H., & Burke, E. A. J. (1990). Fluid inclusions in granulites and eclogites from the Bergen Arcs, Caledonides of W. Norway. *Mineralogical Magazine*, *54*(375), 145–158. https://doi.org/10.1180/minmag.1990.054.375.02

Andersen, T., Austrheim, H., & Burke, E. A. J. (1991). Mineral-fluid-melt interactions in high-pressure shear zones in the Bergen Arcs nappe complex, Caledonides of W. Norway: Implications for the fluid regime in Caledonian eclogite-facies metamorphism. *Lithos*, *27*(3), 187–204. https://doi.org/10.1016/0024-4937(91)90012-A

Andersen, T., Burke, E. A. J., & Austrheim, H. (1989). Nitrogen-bearing, aqueous fluid inclusions in some eclogites from the Western Gneiss Region of the Norwegian Caledonides. *Contributions to Mineralogy and Petrology*, *103*(2), 153–165. https://doi.org/10.1007/BF00378501

Arenas, R. (1991). Opposite P, T, t paths of Hercynian metamorphism between the upper units of the Cabo Ortegal Complex and their substratum (northwest of the Iberian Massif). *Tectonophysics*, *191*(3–4), 347–364. https://doi.org/10.1016/0040-1951(91)90067-3

Bakker, R. J., & Jansen, J. B. H. (1994). A mechanism for preferential H_2O leakage from fluid inclusions in quartz, based on TEM observations. *Contributions to Mineralogy and Petrology*, *116*(1), 7–20. https://doi.org/10.1007/BF00310686

Bebout, G. E. (2007). Metamorphic chemical geodynamics of subduction zones. *Earth and Planetary Science Letters*, *260*(3–4), 373–393. https://doi.org/10.1016/j.epsl.2007.05.050

Bebout, G. E., Fogel, M. L., & Cartigny, P. (2013). Nitrogen: Highly volatile yet surprisingly compatible. *Elements*, *9*(5), 333–338. https://doi.org/10.2113/gselements.9.5.333

Beranoaguirre, A., de Madinabeitia, S. G., Lorda, M. S., Puelles, P., Ábalos, B., & Ibarguchi, J. G. (2020). U–Pb, Hf isotope and REE constraints on high-pressure acid migmatites from the Cabo Ortegal Complex (NW Spain): New evidence of short-duration metamorphism in a Variscan subduction channel. *Lithos*, *372*, 105660. https://doi.org/10.1016/j.lithos.2020.105660

Bernard-Griffiths, J., Peucat, J. J., Cornichet, J., de Léon, M. I. P., & Ibarguchi, J. G. (1985). U- Pb, Nd isotope and REE geochemistry in eclogites from the Cabo Ortegal Complex, Galicia, Spain: An example of REE immobility conserving MORB-like patterns during high-grade metamorphism. *Chemical Geology: Isotope Geoscience*, *52*(2), 217–225.

Bodnar, R. J. (2003). Reequilibration of fluid inclusions. In I. Samson, A. Anderson, & D. Marshall (Eds.), *Short Course Series* (Vol. 32, pp. 213–230). Mineralogical Association of Canada.

Boulard, E., Guyot, F., & Fiquet, G. (2012). The influence on Fe content on Raman spectra and unit cell parameters of magnesite–siderite solid solutions. *Physics and Chemistry of Minerals*, *39*(3), 239–246. https://doi.org/10.1007/s00269-011-0479-3

Busigny, V., Cartigny, P., Philippot, P., Ader, M., & Javoy, M. (2003). Massive recycling of nitrogen and other fluid-mobile elements (K, Rb, Cs, H) in a cold slab environment: Evidence from HP to UHP oceanic metasediments of the Schistes Lustrés nappe (western Alps, Europe). *Earth and Planetary Science Letters*, *215*(1-2), 27–42.

Busigny, V., & Bebout, G. E. (2013). Nitrogen in the silicate Earth: Speciation and isotopic behavior during mineral–fluid interactions. *Elements*, *9*(5), 353–358. https://doi.org/10.2113/gselements.9.5.353

Busigny, V., Cartigny, P., & Philippot, P. (2011). Nitrogen isotopes in ophiolitic metagabbros: A re-evaluation of modern nitrogen fluxes in subduction zones and implication for the early Earth atmosphere. *Geochimica et Cosmochimica Acta*, *75*(23), 7502–7521. https://doi.org/10.1016/j.gca.2011.09.049

Campione, M., Malaspina, N., & Frezzotti, M. L. (2015). Threshold size for fluid inclusion decrepitation. *Journal of Geophysical Research - Solid Earth*, *120*(11), 7396–7402. https://doi.org/10.1002/2015JB012086

Cannaò, E., Tiepolo, M., Bebout, G. E., & Scambelluri, M. (2020). Into the deep and beyond: Carbon and nitrogen subduction recycling in secondary peridotites. *Earth and Planetary Science Letters*, *543*, 116328. https://doi.org/10.1016/j.epsl.2020.116328

Carswell, T., & Compagnoni, R. (2003). Introduction with review of the definition, distribution and geotectonic significance of ultrahigh pressure metamorphism. In T. Carswell & R. Compagnoni (Eds.), *Ultrahigh Pressure Metamorphism, EMU Notes in Mineralogy* (Vol. 5, pp. 3–9). https://doi.org/10.1180/EMU-notes.5.1

Cartigny, P., Harris, J. W., & Javoy, M. (2001). Diamond genesis, mantle fractionations and mantle nitrogen content: a study of δ13C–N concentrations in diamonds. *Earth and Planetary Science Letters*, *185*(1–2), 85–98. https://doi.org/10.1016/S0012-821X(00)00357-5

Cartigny, P., & Marty, B. (2013). Nitrogen isotopes and mantle geodynamics: The emergence of life and the atmosphere–crust–mantle connection. *Elements*, *9*(5), 359–366. https://doi.org/10.2113/gselements.9.5.359

Carvalho, B. B., Bartoli, O., Cesare, B., Tacchetto, T., Gianola, O., Ferri, F., Aradi, L. E., & Szabó, C. (2020). Primary CO_2-bearing fluid inclusions in granulitic garnet usually do not survive. *Earth and Planetary Science Letters*, *536*, 116170. https://doi.org/10.1016/j.epsl.2020.116170

Carvalho, B. B., Bartoli, O., Ferri, F., Cesare, B., Ferrero, S., Remusat, L., Capizzi, L. S., & Poli, S. (2019). Anatexis and fluid regime of the deep continental crust: New clues from melt and fluid inclusions in metapelitic migmatites from Ivrea Zone (NW Italy). *Journal of Metamorphic Geology*, *37*(7), 951–975. https://doi.org/10.1111/jmg.12463

Cedeño, D. G., Conceicao, R. V., de Souza, M. R. W., Quinteiro, R. V. S., Carniel, L. C., Ketzer, J. M. M., Rodrigues, F., & Bruzza, E. C. (2019). An experimental study on smectites as nitrogen conveyors in subduction zones. *Applied Clay Science*, *168*, 409–420. https://doi.org/10.1016/j.clay.2018.11.006

Cesare, B. (1995). Graphite precipitation in C—O—H fluid inclusions: closed system compositional and density changes, and thermobarometric implications. *Contributions to Mineralogy and Petrology*, *122*(1–2), 25–33. https://doi.org/10.1007/s004100050110

Cesare, B., Acosta-Vigil, A., Bartoli, O., & Ferrero, S. (2015). What can we learn from melt inclusions in migmatites and granulites? *Lithos*, *239*, 186–216. https://doi.org/10.1016/j.lithos.2015.09.028

Cesare, B., Maineri, C., Toaldo, A. B., Pedron, D., & Vigil, A. A. (2007). Immiscibility between carbonic fluids and granitic melts during crustal anatexis: a fluid and melt inclusion study in the enclaves of the Neogene Volcanic Province of SE Spain. *Chemical Geology*, *237*(3–4), 433–449. https://doi.org/10.1016/j.chemgeo.2006.07.013

Chaudhuri, H., Ghose, D., Bhandari, R. K., Sen, P., & Sinha, B. (2012). A geochemical approach to earthquake reconnaissance at the Baratang mud volcano, Andaman and Nicobar Islands. *Journal of Asian Earth Sciences*, *46*, 52–60. https://doi.org/10.1016/j.jseaes.2011.10.007

Connolly, J. A. D. (1990). Multivariable Phase-Diagrams - an Algorithm Based on Generalized Thermodynamics. *American Journal of Science*, *290*, 666–718. https://doi.org/10.2475/ajs.290.6.666

Connolly, J. A. D. (1995). Phase diagram methods for graphitic rocks and application to the system C-O-H-FeO-TiO_2-SiO_2. *Contributions to Mineralogy and Petrology*, *119*(1), 94–116. https://doi.org/10.1007/BF00310720

Connolly, J. A. D. (2009). The geodynamic equation of state: What and how. *Geochemistry, Geophysics, Geosystems*, *10*, 1–19. https://doi.org/10.1029/2009GC002540

Connolly, J. A. D., & Galvez, M. E. (2018). Electrolytic Fluid Speciation by Gibbs Energy Minimization and Implications for Subduction Zone Mass Transfer. *Earth and Planetary Science Letters*, *501*, 90–102. https://doi.org/10.1016/j.epsl.2018.08.024

Den Tex, E. (1961). Some preliminary result of petrological work in Galicia (NW Spain). *Leidse Geologische Mededelingen*, *206*, 75–91.

Diamond, L. W. (2001). Review of the systematics of CO2–H2O fluid inclusions. *Lithos*, *55*(1–4), 69–99. https://doi.org/10.1016/S0024-4937(00)00039-6

Dolejš, D., & Manning, C. E. (2010). Thermodynamic model for mineral solubility in aqueous fluids: theory, calibration and application to model fluid-flow systems. *Geofluids*, *10*(1–2), 20–40. https://doi.org/10.1002/9781444394900.ch3

Ferrando, S., Frezzotti, M. L., Dallai, L., & Compagnoni, R. (2005). Multiphase solid inclusions in UHP rocks (Su-Lu, China): Remnants of supercritical silicate-rich aqueous fluids released during continental subduction. *Chemical Geology*, *223*(1–3), 68–81. https://doi.org/10.1016/j.chemgeo.2005.01.029

Ferrero, S., Braga, R., Berkesi, M., Cesare, B., & Laridhi Ouazaa, N. (2014). Production of metaluminous melt during fluid-present anatexis: an example from the Maghrebian basement, La Galite Archipelago, central Mediterranean. *Journal of Metamorphic Geology*, *32*(2), 209–225. https://doi.org/10.1111/jmg.12068

Fischer, T. P., Hilton, D. R., Zimmer, M. M., Shaw, A. M., Sharp, Z. D., & Walker, J. A. (2002). Subduction and recycling of nitrogen along the Central American margin. *Science*, *297*(5584), 1154–1157. https://doi.org/10.1126/science.1073995

Frezzotti, M. L., & Ferrando, S. (2007). Multiphase solid inclusions in ultra-high pressure metamorphic rocks: A petrographic approach. *Per. Mineral.*, *76*, 113–125.

Frezzotti, M. L., & Ferrando, S. (2015). The chemical behavior of fluids released during deep subduction based on fluid inclusions. *American Mineralogist*, *100*(2–3), 352–377.

Frezzotti, M. L., Ferrando, S., Tecce, F., & Castelli, D. (2012). Water content and nature of solutes in shallow-mantle fluids from fluid inclusions. *Earth and Planetary Science Letters*, *351*, 70–83.

Fu, B., Touret, J. L. R., & Zheng, Y. F. (2003). Remnants of premetamorphic fluid and oxygen isotopic signatures in eclogites and garnet clinopyroxenite from the Dabie-Sulu terranes, eastern China. *Journal of Metamorphic Geology*, *21*(6), 561–578.

Galvez, M. E., Beyssac, O., Martinez, I., Benzerara, K., Chaduteau, C., Malvoisin, B., & Malavieille, J. (2013). Graphite formation by carbonate reduction during subduction. *Nature Geoscience*, *6*, 473–477. https://doi.org/10.1038/ngeo1827

Galvez, M. E., Connolly, J. A. D., & Manning, C. E. (2016). Implications for metal and volatile cycles from the pH of subduction zone fluids. *Nature*. Macmillan Publishers Limited, part of Springer Nature. All rights reserved. 539, 420, *539*, 420–424. https://doi.org/10.1038/nature20103

Gerya, T. (2019). *Introduction to Numerical Geodynamic Modelling*. Cambridge University Press. 454 p

Giggenbach, W. F., Sano, Y., & Wakita, H. (1993). Isotopic composition of helium, and CO_2 and CH_4 contents in gases produced along the New Zealand part of a convergent plate boundary. *Geochimica et Cosmochimica Acta*, *57*(14), 3427–3455.

Gil Ibarguchi, J. I., Ábalos, B., Azcarraga, J., & Puelles, P. (1999). Deformation, high-pressure metamorphism and exhumation of ultramafic rocks in a deep subduction/collision setting (Cabo Ortegal, NW Spain). *Journal of Metamorphic Geology*, *17*(6), 747–764.

Gil Ibarguchi, J. I., Mendia, M., Girardeau, J., & Peucat, J. J. (1990). Petrology of eclogites and clinopyroxene-garnet metabasites from the Cabo Ortegal Complex (northwestern Spain). *Lithos*, *25*(1–3), 133–162.

Gillet, P., Biellmann, C., Reynard, B., & McMillan, P. (1993). Raman spectroscopic studies of carbonates Part I: High-pressure and high-temperature behaviour of calcite, magnesite, dolomite and aragonite. *Physics and Chemistry of Minerals*, *20*(1), 1–18.

Girardeau, J., & Gil Ibarguchi, J. I. (1991). Pyroxenite-rich peridotites of the Cabo Ortegal complex (Northwestern Spain): evidence for large-scale upper-mantle heterogeneity. *Journal of Petrology*, *2*, 135–154.

Halama, R., Bebout, G. E., John, T., & Scambelluri, M. (2012). Nitrogen recycling in subducted mantle rocks and implications for the global nitrogen cycle. *International Journal of Earth Sciences*, *103*(7), 2081–2099.

Halama, R., Bebout, G. E., John, T., & Schenk, V. (2010). Nitrogen recycling in subducted oceanic lithosphere: the record in high- and ultrahigh-pressure metabasaltic rocks. *Geochimica et Cosmochimica Acta*, *74*(5), 1636–1652.

Hall, D. L., & Bodnar, R. J. (1990). Methane in fluid inclusions from granulites: A product of hydrogen diffusion? *Geochimica et Cosmochimica Acta*, *54*(3), 641–651.

Hall, D. L., & Sterner, S. M. (1993). Preferential water loss from synthetic fluid inclusions. *Contributions to Mineralogy and Petrology*, *114*(4), 489–500.

Haskin, L. A., Wang, A., Rockow, K. M., Jolliff, B. L., Korotev, R. L., & Viskupic, K. M. (1997). Raman spectroscopy for mineral identification and quantification for in situ planetary surface analysis: A point count method. *Journal of Geophysical Research, Planets*, *102*(E8), 19293–19306.

Henry, H., Tilhac, R., Griffin, W. L., O'Reilly, S. Y., Satsukawa, T., Kaczmarek, M. A., Grégoire, M., & Ceuleneer, G. (2017). Deformation of Mantle Pyroxenites Provides Clues to Geodynamic Processes in Subduction Zones: Case Study of the Cabo Ortegal Complex, Spain. *Earth and Planetary Science Letters*, *472*, 174–185. https://doi.org/10.1016/j.epsl.2017.05.028

Hermann, J., Spandler, C., Hack, A., & Korsakov, A. V. (2006). Aqueous fluids and hydrous melts in high-pressure and ultra-high pressure rocks: implications for element transfer in subduction zones. *Lithos*, *92*(3–4), 399–417.

Hermann, J., Zheng, Y. F., & Rubatto, D. (2013). Deep fluids in subducted continental crust. *Elements*, *9*(4), 281–287.

Hidas, K., Guzmics, T., Szabó, C., Kovács, I., Bodnar, R. J., Zajacz, Z., Nédli, Z., Vaccari, L., & Perucchi, A. (2010). Coexisting silicate melt inclusions and H_2O-bearing, CO_2-rich fluid inclusions in mantle peridotite xenoliths from the Carpathian–Pannonian region (central Hungary). *Chemical Geology*, *274*(1–2), 1–18.

Holland, T. J. B. (1979). Experimental determination of the reaction paragonite = jadeite+ kyanite+ H_2O, and internally consistent thermodynamic data for part of the system $Na_2O - Al_2O_3 - SiO_2 - H_2O$, with applications to eclogites and blueschists. *Contributions to Mineralogy and Petrology*, *68*(3), 293–301.

Holland, T. J. B., & Powell, R. (2011). An improved and extended internally consistent thermodynamic dataset for phases of petrological interest, involving a new equation of state for solids. *Journal of Metamorphic Geology*, *29*(3), 333–383.

Hurai, V. (2010). Fluid inclusion geobarometry: Pressure corrections for immiscible H2O–CH4 and H_2O–CO_2 fluids. *Chemical Geology*, *278*(3–4), 201–211.

Jamtveit, B., Bucher-Nurminen, K., & Austrheim, H. (1990). Fluid controlled eclogitization of granulites in deep crustal shear zones, Bergen arcs, Western Norway. *Contributions to Mineralogy and Petrology*, *104*(2), 184–193.

Kendrick, M. A., Scambelluri, M., Hermann, J., & Padrón-Navarta, J. A. (2018). Halogens and noble gases in serpentinites and secondary peridotites: Implications for seawater subduction and the origin of mantle neon. *Geochimica et Cosmochimica Acta*, *235*, 285–304.

Kendrick, M. A., Scambelluri, M., Honda, M., & Phillips, D. (2011). High abundances of noble gas and chlorine delivered to the mantle by serpentinite subduction. *Nature Geoscience*. Nature Publishing Group, a division of Macmillan Publishers Limited. All Rights Reserved, *4*, 807–812. https://doi.org/10.1038/ngeo1270

Kessel, R., Schmidt, M. W., Ulmer, P., & Pettke, T. (2005). Trace element signature of subduction-zone fluids, melts and supercritical liquids at 120–180 km depth. *Nature*, *437*(7059), 724–727. https://doi.org/10.1038/nature03971

Kessel, R., Ulmer, P., Pettke, T., Schmidt, M. W., & Thompson, A. B. (2004). A novel approach to determine high-pressure high-temperature fluid and melt compositions using diamond-trap experiments. *American Mineralogist*, *89*(7), 1078–1086.

Korsakov, A. V., & Hermann, J. (2006). Silicate and carbonate melt inclusions associated with diamonds in deeply subducted carbonate rocks. *Earth and Planetary Science Letters*, *241*(1–2), 104–118.

Lee, H., Fischer, T. P., de Moor, J. M., Sharp, Z. D., Takahata, N., & Sano, Y. (2017). Nitrogen recycling at the Costa Rican subduction zone: The role of incoming plate structure. *Scientific Reports*, *7*(1), 1–10. https://doi.org/10.1038/s41598-017-14287-y

Li, Y., & Keppler, H. (2014). Nitrogen speciation in mantle and crustal fluids. *Geochimica et Cosmochimica Acta*, *129*, 13–32.

Llana-Fúnez, S., & Brown, D. (2012). Contribution of Crystallographic Preferred Orientation to Seismic Anisotropy across a Surface Analog of the Continental Moho at Cabo Ortegal, Spain. *GSA Bulletin*, *124*(9–10), 1495–1513. https://doi.org/10.1130/B30568.1

Maffeis, A., Ferrando, S., Connolly, J. A. D., Groppo, C., Frezzotti, M. L., & Castelli, D. (2021). Thermodynamic analysis of HP-UHP fluid inclusions: The solute load and chemistryof metamorphic fluids. *Geochimica et Cosmochimica Acta*, *315*, 207–229. https://doi.org/10.1016/j.gca.2021.08.044

Manning, C. E. (1994). The solubility of quartz in H_2O in the lower crust and upper mantle. *Geochimica et Cosmochimica Acta*, *58*(22), 4831–4839.

Manning, C. E. (2004). The chemistry of subduction-zone fluids. *Earth and Planetary Science Letters*, *223*(1–2), 1–16. https://doi.org/10.1016/j.epsl.2004.04.030

Marcos, A., Farias, P., Galán, G., Fernández, F. J., & Llana-Fúnez, S. (2002). Tectonic framework of the Cabo Ortegal Complex: A slab of lower crust exhumed in the Variscan orogen (northwestern Iberian Peninsula). *Special Papers-Geological Society Of America*, *364*, 143–162. https://doi.org/10.1130/0-8137-2364-7.143

Marini, L. (2007). *Geological Sequestration of Carbon Dioxide: Thermodynamics, Kinetics, and Reaction Path Modeling* (Vol. 11). Elsevier. 470 p

Martínez Catalán, J. R., Arenas, R., Abati, J., Martínez, S. S., García, F. D., Suárez, J. F., Cuadra, P. G., Castiñeiras, P., Barreiro, J. G., Montes, A. D., Clavijo, E. G., Pascual, F. J. R., Andonaegui, P., Jeffries, T. E., Alcock, J. E., Díez Fernández, R. D., & Carmona, A. L. (2009). A rootless suture and the loss of the roots of a mountain chain: the Variscan belt of NW Iberia. *Comptes Rendus Geoscience*, *341*(2–3), 114–126.

Mavrogenes, J. A., & Bodnar, R. J. (1994). Hydrogen movement into and out of fluid inclusions in quartz: Experimental evidence and geologic implications. *Geochimica et Cosmochimica Acta*, *58*(1), 141–148.

Mendia, M. S. (2000). Petrología de la unidad eclogítica del Complejo de Cabo Ortegal (NW de España). Serie Nova Terra 16 (La Coruña).

Menzel, M. D., Garrido, C. J., Sánchez-Vizcaíno, V. L., Marchesi, C., Hidas, K., Escayola, M. P., & Huertas, A. D. (2018). Carbonation of mantle peridotite by CO_2-rich fluids: the formation of listvenites in the Advocate ophiolite complex (Newfoundland, Canada). *Lithos*, *323*, 238–261.

Mikhail, S., & Sverjensky, D. A. (2014). Nitrogen speciation in upper mantle fluids and the origin of Earth's nitrogen-rich atmosphere. *Nature Geoscience*, *7*, 816–819. https://doi.org/10.1038/ngeo2271

Mitchell, E. C., Fischer, T. P., Hilton, D. R., Hauri, E. H., Shaw, A. M., de Moor, J. M., Sharp, Z. D., & Kazahaya, K. (2010). Nitrogen sources and recycling at subduction zones: Insights from the Izu-Bonin-Mariana arc. *Geochemistry, Geophysics, Geosystems*, *11*(2), 1–24. https://doi.org/10.1029/2009GC002783

Motyka, R. J., Poreda, R. J., & Jeffrey, A. W. (1989). Geochemistry, isotopic composition, and origin of fluids emanating from mud volcanoes in the Copper River basin, Alaska. *Geochimica et Cosmochimica Acta*, *53*(1), 29–41.

Mukherjee, B. K., & Sachan, H. K. (2009). Fluids in coesite-bearing rocks of the Tso Morari Complex, NW Himalaya: evidence for entrapment during peak metamorphism and subsequent uplift. *Geological Magazine*, *146*(6), 876–889.

Mysen, B. (2019). Nitrogen in the Earth: abundance and transport. *Progress in Earth and Planetary Science*, *6*(1), 1–15.

Newton, R. C., & Manning, C. E. (2003). Activity coefficient and polymerization of aqueous silica at 800 C, 12 kbar, from solubility measurements on SiO 2-buffering mineral assemblages. *Contributions to Mineralogy and Petrology*, *146*(2), 135–143.

Newton, R. C., & Manning, C. E. (2010). Role of saline fluids in deep-crustal and upper-mantle metasomatism: insights from experimental studies. *Geofluids*, *10*(1-2), 58–72.

Ni, H., Zhang, L., Xiong, X., Mao, Z., & Wang, J. (2017). Supercritical fluids at subduction zones: evidence, formation condition, and physicochemical properties. *Earth-Science Reviews*, *167*, 62–71.

Novo-Fernández, I., Garcia-Casco, A., Arenas, R., & Díez Fernández, R. (2016). The metahyaloclastitic matrix of a unique metavolcanic block reveals subduction in the Somozas Mélange (Cabo Ortegal Complex, NW Iberia): tectonic implications for the assembly of Pangea. *Journal of Metamorphic Geology*, *34*(9), 963–985.

Ordóñez Casado, B. O., Gebauer, D., Schäfer, H. J., Gil Ibarguchi, J. I., & Peucat, J. J. (2001). A single Devonian subduction event for the HP/HT metamorphism of the Cabo Ortegal complex within the Iberian Massif. *Tectonophysics*, *332*(3), 359–385.

Peng, W., Zhang, L., Menzel, M. D., Brovarone, A. V., Tumiati, S., Shen, T., & Hu, H. (2020). Multistage CO_2 sequestration in the subduction zone: Insights from exhumed carbonated serpentinites, SW Tianshan UHP belt, China. *Geochimica et Cosmochimica Acta*, *270*, 218–243.

Peucat, J. J., Bernard-Griffiths, J., Ibarguchi, J. G., Dallmeyer, R. D., Menot, R. P., Cornichet, J., & De Leon, M. I. P. (1990). Geochemical and geochronological cross section of the deep Variscan crust: The Cabo Ortegal high-pressure nappe (northwestern Spain). *Tectonophysics*, *177*(1–3), 263–292.

Philippot, P., Busigny, V., Scambelluri, M., & Cartigny, P. (2007). Oxygen and nitrogen isotopes as tracers of fluid activities in serpentinites and metasediments during subduction. *Mineralogy and Petrology*, *91*(1–2), 11–24.

Philippot, P., & Selverstone, J. (1991). Trace-element-rich brines in eclogitic veins: implications for fluid composition and transport during subduction. *Contributions to Mineralogy and Petrology*, *106*(4), 417–430.

Piccoli, F., Brovarone, A. V., Beyssac, O., Martinez, I., Ague, J. J., & Chaduteau, C. (2016). Carbonation by fluid–rock interactions at high-pressure conditions: implications for carbon cycling in subduction zones. *Earth and Planetary Science Letters*, *445*, 146–159.

Poli, S., & Schmidt, M. W. (2002). Petrology of subducted slabs. *Annual Review of Earth and Planetary Sciences*, *30*(1), 207–235.

Puelles, P., Ábalos, B., & Ibarguchi, J. G. (2005). Metamorphic evolution and thermobaric structure of the subduction-related Bacariza high-pressure granulite formation (Cabo Ortegal Complex, NW Spain). *Lithos*, *84*(1–2), 125–149.

Puelles, P., Ábalos, B., & Ibarguchi, J. G. (2009). Transposed high-pressure granulite fabrics (Cabo Ortegal, NW Spain): Implications on the scales of deformation localization. *Journal of Structural Geology*, *31*(8), 776–790.

Rividi, N., van Zuilen, M., Philippot, P., Menez, B., Godard, G., & Poidatz, E. (2010). Calibration of carbonate composition using micro-Raman analysis: application to planetary surface exploration. *Astrobiology*, *10*(3), 293–309.

Roedder, E. (1984). Volume 12: Fluid inclusions. *Reviews in Mineralogy*, *12*, 644.

Rutt, H. N., & Nicola, J. H. (1974). Raman spectra of carbonates of calcite structure. *Journal of Physics C: Solid State Physics*, *7*(24), 4522–4528. https://doi.org/10.1088/0022-3719/7/24/015

Sano, Y., Takahata, N., Nishio, Y., Fischer, T. P., & Williams, S. N. (2001). Volcanic flux of nitrogen from the Earth. *Chemical Geology*, *171*(3–4), 263–271.

Santos Zalduegui, J. F., Schärer, U., Gil Ibarguchi, J. I., & Girardeau, J. (2002). Genesis of pyroxenite-rich peridotite at Cabo Ortegal (NW Spain): geochemical and Pb–Sr–Nd isotope data. *Journal of Petrology*, *43*(1), 17–43.

Scambelluri, M., Bebout, G. E., Belmonte, D., Gilio, M., Campomenosi, N., Collins, N., & Crispini, L. (2016). Carbonation of subduction-zone serpentinite (high-pressure ophicarbonate; Ligurian Western Alps) and implications for the deep carbon cycling. *Earth and Planetary Science Letters*, *441*, 155–166.

Scambelluri, M., & Philippot, P. (2001). Deep fluids in subduction zones. *Lithos*, *55*(1–4), 213–227.

Schrötter, H. W., & Klöckner, H. W. (1979). Raman scattering cross sections in gases and liquids. In A. Weber (Ed.), *Raman Spectroscopy of Gases and Liquids* (pp. 123–166). Springer.

Snyder, G., Poreda, R., Fehn, U., & Hunt, A. (2003). Sources of nitrogen and methane in Central American geothermal settings: Noble gas and 129I evidence for crustal and magmatic volatile components. *Geochemistry, Geophysics, Geosystems*, *4*(1), 1–28.

Tacchetto, T., Bartoli, O., Cesare, B., Berkesi, M., Aradi, L. E., Dumond, G., & Szabó, C. (2019). Multiphase inclusions in peritectic garnet from granulites of the Athabasca granulite terrane (Canada): Evidence of carbon recycling during Neoarchean crustal melting. *Chemical Geology*, *508*, 197–209.

Tao, R., Zhang, L., Tian, M., Zhu, J., Liu, X., Liu, J., Höfer, H. E., Stagno, V., & Fei, Y. (2018). Formation of abiotic hydrocarbon from reduction of carbonate in subduction zones: Constraints from petrological observation and experimental simulation. *Geochimica et Cosmochimica Acta*, *239*, 390–408.

Tilhac, R., Ceuleneer, G., Griffin, W. L., O'Reilly, S. Y., Pearson, N. J., Benoit, M., Henry, H., Girardeau, J., & Grégoire, M. (2016). Primitive arc magmatism and delamination: petrology and geochemistry of Pyroxenites from the Cabo Ortegal Complex, Spain. *Journal of Petrology*, *57*(10), 1921–1954.

Tilhac, R., Grégoire, M., O'Reilly, S. Y., Griffin, W. L., Henry, H., & Ceuleneer, G. (2017). Sources and timing of pyroxenite formation in the sub-arc mantle: Case study of the Cabo Ortegal Complex, Spain. *Earth and Planetary Science Letters*, *474*, 490–502.

Tilhac, R., Oliveira, B., Griffin, W. L., O'Reilly, S. Y., Schaefer, B. F., Alard, O., Ceuleneer, G., Afonso, J. C., & Grégoire, M. (2020). Reworking of old continental lithosphere: Unradiogenic Os and decoupled Hf-Nd isotopes in sub-arc mantle pyroxenites. *Lithos*, *354-355*, 105346. https://doi.org/10.1016/j.lithos.2019.105346

Tiraboschi, C., Tumiati, S., Sverjensky, D., Pettke, T., Ulmer, P., & Poli, S. (2018). Experimental determination of magnesia and silica solubilities in graphite-saturated and redox-buffered high-pressure COH fluids in equilibrium with forsterite + enstatite and magnesite + enstatite. *Contributions to Mineralogy and Petrology*, *173*, 1–17. https://doi.org/10.1007/s00410-017-1427-0

Tomilenko, A. A., & Chupin, V. P. (1983). Thermobarogeochemistry of metamorphic formations (in Russian) Acad. Sci. SSSR Siberian Branch, 542,200 pp.

Torres-Roldán, R. L., & Garcia-Sanchez, P. A. (2000). CSpace: an integrated workplace for the graphical and algebraic analysis of phase assemblages on 32-bit wintel platforms. *Computers & Geosciences*, *26*, 779–793.

Touret, J. (1981). Fluid inclusions in high-grade metamorphic rocks. In L. S. Hollister & M. L. Crawford (Eds.), *Short Course in Fluid Inclusions: Application to Petrology* (pp. 182–208). Mineral Association of Canada.

Touret, J. L., & Frezzotti, M. L. (2003). Fluid inclusions in high pressure and ultrahigh pressure metamorphic rocks. In *Ultrahigh pressure metamorphism, EMU Notes in Mineralogy* (Vol. 5) (pp. 467–487). Eötvös University Press Budapest.

Touret, J. L. R. (2001). Fluids in metamorphic rocks. *Lithos*, *55*(1–4), 1–25.

Vitale Brovarone, A., Sverjensky, D. A., Piccoli, F., Ressico, F., Giovannelli, D., & Daniel, I. (2020). Subduction hides high-pressure sources of energy that may feed the deep subsurface biosphere. *Nature Communications*, *11*(1), 1–11.

Viti, C., & Frezzotti, M. L. (2001). Transmission electron microscopy applied to fluid inclusion investigations. *Lithos*, *55*(1–4), 125–138.

Vogel, D. E. (1967). Petrology of an eclogite-and pyrigarnite-bearing polymetamorphic rock complex at Cabo Ortegal, NW Spain. *Leidse Geologische Mededelingen*, *40*(1), 121–213.

Wang, A., Freeman, J. J., & Jolliff, B. L. (2015). Understanding the Raman spectral features of phyllosilicates. *Journal of Raman Spectroscopy*, *46*(10), 829–845.

Watenphul, A., Wunder, B., & Heinrich, W. (2009). High-pressure ammonium-bearing silicates: Implications for nitrogen and hydrogen storage in the Earth's mantle. *American Mineralogist*, *94*(2–3), 283–292.

Whitney, D. L., & Evans, B. W. (2010). Abbreviations for names of rock-forming minerals. *American Mineralogist*, *95*, 185–187.

Yamamoto, J., Otsuka, K., Ohfuji, H., Ishibashi, H., Hirano, N., & Kagi, H. (2011). Retentivity of CO_2 in fluid inclusions in mantle minerals. *European Journal of Mineralogy*, *23*(5), 805–815.

Zheng, Y. F. (2019). Subduction zone geochemistry. *Geoscience Frontiers*, *10*(4), 1223–1254. https://doi.org/10.1016/j.gsf.2019.02.003

Zheng, Y. F., & Hermann, J. (2014). Geochemistry of continental subduction-zone fluids. *Earth, Planets and Space*, *66*(1), 1–16.

SUPPORTING INFORMATION

Additional supporting information may be found in the online version of the article at the publisher's website.

Appendix S1. Detailed description of the applied analytical methods: SEM-EDS, Raman spectroscopy, FIB-SEM and thermodynamic modelling.

Appendix S2. Molar volumes used to estimate MFI bulk composition.

Appendix S3. Calculation of a potential original composition of the fluid in equilibrium with the eclogite.

Figure S1. A pseudosection and the iso-values for CO_2 in equilibrium with the eclogite to specify the effect of CO_2 addition on the mineral assemblages at peak conditions (dashed grey line), calculated based on bulk rock data of Gil Ibarguchi et al. (1990), for details see text and Appendix S3. Modal proportions, mineral composition and phase speciation of stable phases are presented in Table S14–15.

Figure S2. Representative Raman spectra of solid (calcite and talc) and fluid phases (nitrogen and methane) in MFI in clinopyroxene of pyroxenite from the COC.

Figure S3. a-b-c) Representative EDS spectra of dominant solid phases of the MFI in the studied eclogite and granulites obtained during FIB sectioning.

Figure S4. Pseudosection of a representative multiphase fluid inclusion in ultramafic granulite using the bulk composition of MFI_FIB3, shown on Figure 9. The stability fields of carbonates, pyrophyllite and garnet are

indicated (with colored lines). Color blue levels indicate the variance of the assemblage (the darker the higher the variance). Carb designates the presence/abscence of any of the two carbonates.

Table S1. Relative proportions (in mol%) of fluid phases determined by Raman spectroscopy inside unexposed MFI in the studied rocks, presented on Figure 5.

Table S2. Mineral chemistry of the measured solid phases (carbonates, pyrophyllite and chlorite) in exposed MFI and the host mineral (garnet) of eclogite (COC17-062) and ultramafic granulite (COC17-079a) based SEM-EDS data.

Table S3. Volume (vol.%) and modal (area%) proportion of solid and fluid phases (raw data) in MFI of eclogite (COC17-062) and ultramafic granulite (COC17-079a) obtained with FIB-SEM analyses (eclogite: MFI_FIB1–2 and granulite: MFI_FIB3) and Raman imaging (eclogite: MFI#1–30 and granulite: MFI#31–39), respectively.

Table S4. Modal (area%) proportion of solid and fluid phases (extrapolated to vol.% and normalized to 100%) in MFI of eclogite (COC17-062) and ultramafic granulite (COC17-079a) obtained with FIB-SEM analyses (eclogite: MFI_FIB1–2 and granulite: MFI_FIB3) and Raman imaging (eclogite: MFI#1–30 and granulite: MFI#31–39), respectively. Density was calculated (see Table S7) according to estimation of residual pressure in the MFI using characteristic peak positions of the fluids, for details, see Appendix S2.

Table S5. Volume per kg of system (cm^3) of solid and fluid phases in MFI of eclogite (COC17-062) and ultramafic granulite (COC17-079a) obtained with FIB-SEM analyses (eclogite: MFI_FIB1–2 and granulite: MFI_FIB3) and Raman imaging (eclogite: MFI#1–30 and granulite: MFI#31–39), respectively.

Table S6. Mol per kg of system (cm^3) of solid and fluid phases in MFI of eclogite (COC17-062) and ultramafic granulite (COC17-079a) obtained with FIB-SEM analyses (eclogite: MFI_FIB1–2 and granulite: MFI_FIB3) and Raman imaging (eclogite: MFI#1–30 and granulite: MFI#31–39), respectively.

Table S7. Fluid density calculated based on fluid mol% in MFI of eclogite (COC17-062) and ultramafic granulite (COC17-079a) obtained with FIB-SEM analyses (eclogite: MFI_FIB1–2 and granulite: MFI_FIB3) and Raman imaging (eclogite: MFI#1–30 and granulite: MFI#31–39), respectively.

Table S8. Compositional space and compositional corrected estimated densities. The densities of the fluid phases are computed at 500 bar and room temperature (see Appendix S2 for details).

Table S9. Bulk composition of the system in mol/kg of MFI of eclogite (COC17-062) and ultramafic granulite (COC17-079a) obtained with FIB-SEM analyses (eclogite: MFI_FIB1–2 and granulite: MFI_FIB3) and Raman imaging (eclogite: MFI#1–30 and granulite: MFI#31–39), respectively.

Table S10. Modal proportion of the fluids with Raman band positions in MFI in eclogite (COC17–062) applied for estimation the residual pressure in the inclusion.

Table S11. Modal proportion of the fluids with Raman band positions in MFI in ultramafic granulite (COC17-079a) applied for estimation the residual pressure in the inclusion.

Table S12. Modal proportions, mineral composition and phase speciation of stable phases modelled using molecular modelling of MFI_FIB1 bulk composition at both low and high P–T conditions, as indicated with green and yellow stars on Figure 10, respectively.

Table S13. Fluid speciation using electrolytic modelling of MFI_FIB1 bulk composition at both low and high P–T conditions, as indicated with green and yellow stars on Figure 10, respectively. For modal proprotions, mineral composition and phase speciation of stable phases see Table 3.

Table S14. The results of electrolytic modelling using eclogite bulk composition (sample 97 from Gil Ibarguchi et al., 1990) with CO_2-free and high CO_2 concentrations: modal proportions and mineral compositions of the phases modelled at high P–T conditions ($T = 800°C$ and $P = 18$ kbar) - a reasonable approximation for entrapment. For details see text Appendix S3. and Figure S1. Composition of the phases are in atoms per formula unit (apfu), except for the fluid phase, whereas wt.% is additionally indicated in columns with F*.

Table S15. Fluid speciation using electrolytic modelling of eclogite bulk composition (sample 97 from Gil Ibarguchi et al., 1990) with CO_2-free and high CO_2 concentrations: modal proportions and mineral compositions of the phases modelled at high P–T conditions ($T = 800°C$ and $P = 18$ kbar) - a reasonable approximation for entrapment. For details see text Appendix S3. and Figure S1.

How to cite this article: Spránitz, T., Padrón-Navarta, J. A., Szabó, C., Szabó, Á., & Berkesi, M. (2022). Abiotic passive nitrogen and methane enrichment during exhumation of subducted rocks: Primary multiphase fluid inclusions in high-pressure rocks from the Cabo Ortegal Complex, NW Spain. *Journal of Metamorphic Geology*, 1–29. https://doi.org/10.1111/jmg.12666